

---

# GENERALIZING IMAGING BIOMARKER REPEATABILITY STUDIES USING BAYESIAN INFERENCE: APPLICATIONS IN DETECTING HETEROGENEOUS TREATMENT RESPONSE IN WHOLE-BODY DIFFUSION-WEIGHTED MRI OF METASTATIC PROSTATE CANCER

---

A PREPRINT

Matthew D Blackledge<sup>1,\*</sup>, Konstantinos Zormpas-Petridis<sup>2,3</sup>, Ricardo Donners<sup>1,4</sup>, Antonio Candito<sup>1</sup>, David J Collins<sup>1,5</sup>, Johann de Bono<sup>1,5</sup>, Chris Parker<sup>1,5</sup>, Dow-Mu Koh<sup>1,5</sup>, and Nina Tunariu<sup>1,5</sup>

<sup>1</sup>The Institute of Cancer Research, London, United Kingdom

<sup>2</sup>Fondazione Policlinico Universitario Agostino Gemelli IRCCS, Rome, Italy

<sup>3</sup>Università Cattolica del Sacro Cuore, Rome, Italy

<sup>4</sup>Universitätsspital Basel, Basel, Switzerland

<sup>5</sup>The Royal Marsden NHS Foundation Trust, London, United Kingdom

\*Correspondence: matthew.blackledge@icr.ac.uk; 15 Cotswold Road, Sutton, SM2 5NG, United Kingdom

## ABSTRACT

The assessment of imaging biomarkers is critical for advancing precision medicine and improving disease characterization. Despite the availability of methods to derive disease heterogeneity metrics in imaging studies, a robust framework for evaluating measurement uncertainty remains underdeveloped. To address this gap, we propose a novel Bayesian framework to assess the precision of disease heterogeneity measures in biomarker studies.

Our approach extends traditional methods for evaluating biomarker precision by providing greater flexibility in statistical assumptions and enabling the analysis of biomarkers beyond univariate or multivariate normally-distributed variables. Using Hamiltonian Monte Carlo (HMC) sampling, the framework supports both, for example, normally-distributed and Dirichlet-Multinomial distributed variables, enabling the derivation of posterior distributions for biomarker parameters under diverse model assumptions. Designed to be broadly applicable across various imaging modalities and biomarker types, the framework builds a foundation for generalizing reproducible and objective biomarker evaluation.

To demonstrate its utility, we apply the framework to whole-body diffusion-weighted MRI (WBDWI) to assess heterogeneous therapeutic responses in metastatic bone disease. Specifically, we analyze data from two patient studies investigating treatments for metastatic castrate-resistant prostate cancer (mCRPC). Mixed therapeutic responses, recognized as a sign of disease heterogeneity with potential adverse clinical implications, are part of the Prostate Cancer Working Group 3.0 criteria. Our results reveal an approximately 70% response rate among individual tumors across both studies, objectively characterizing differential responses to systemic therapies and validating the clinical relevance of the proposed methodology.

This Bayesian framework provides a powerful tool for advancing biomarker research across diverse imaging-based studies while offering valuable insights into specific clinical applications, such as mCRPC treatment response.

**Keywords** Imaging Biomarkers · Bayesian Inference · Diffusion-Weighted MRI · Prostate Cancer

## 1 Introduction

There is a clear trend that medical imaging is becoming more quantitative; images are not only being used for qualitative radiological evaluation, but more frequently to derive *imaging biomarkers* (IBs) that act as non-invasive surrogate measurements of biological and/or pathogenic characteristics of the imaged tissue Gillies et al. [2016], O’Connor et al. [2017]. An example of a widely used biomarker in oncology is tumour size measurement defined by RECIST, where the sum of the longest diameters in up to five target lesions (maximum two per organ) is recorded and monitored throughout the patient treatment pathway Eisenhauer et al. [2009]. As imaging technologies advance and acquisition times accelerate, this has facilitated increased data collection to derive multiple IBs in a single patient study. For example, magnetic resonance imaging (MRI) offers measurement of tumour cellularity with diffusion-weighted imaging (DWI) Charles-Edwards and deSouza [2006], Koh and Collins [2007], Surov et al. [2017], tissue stiffness using elastography (MRE) Manduca et al. [2021], Sack [2023], and tumour vasculature through dynamic contrast-enhanced imaging (DCE) Leach et al. [2012], Sujlana et al. [2018].

Whilst this presents practical challenges to radiologists needing to evaluate more images per patient study, it also offers multi-faceted insight into how the tumour microenvironment responds to therapy Hoffmann et al. [2024]. Cancer is an intrinsically complex, heterogeneous and evolving disease McGranahan and Swanton [2015]. Within such an ecosystem, molecularly and morphologically-distinct tumour regions (“habitats”) interact and adapt differently to selection pressures (including therapy) to gain evolutionary fitness advantages Maley et al. [2017], Amend and Pienta [2015]. These changes may differ between spatially isolated sites of disease (inter-lesion heterogeneity) or indeed within a single lesion (intra-lesion heterogeneity). Recent techniques have been developed to combine features from multiple quantitative imaging biomarkers and identify these spatially distinct regions, while validating these features using ex-vivo histopathological assessment Sala et al. [2017], Crispin-Ortuzar et al. [2020], Beer et al. [2021], Zormpas-Petridis et al. [2020]. A key advantage of such habitat mapping is that it can cover the entire tumour volume and non-invasively monitor changes in the habitats across treatment. This is in stark contrast to tissue biopsies, which although offer great biological detail, cannot sample every location within the tumour and is therefore unable to reflect the full range of tissue characteristics before and after treatment Panico et al. [2023]. The habitats derived from such techniques can be viewed as representing new forms of imaging biomarkers that equally require validation if they are to be used in the clinic.

An important question remains as to how to best treat quantification of habitats and their change over treatment within the statistical framework of imaging biomarkers. For example, a vital characteristic of any IB intended to monitor cancer response is that it be robust and precise Obuchowski [2018], Obuchowski and Buckler [2022]. If the IB measurement is found to be highly sensitive to imaging/patient set-up, statistical image noise, or operator variability, then it might be that the IB is not sensitive or robust enough to detect subtle changes occurring within tumours. The importance of IB precision has been highlighted in the Cancer Research UK (CRUK) and the European Organisation for Research and Treatment of Cancer (EORTC) IB roadmap O’Connor et al. [2017], where evaluation of measurement precision is a core requirement at every step of technical validation, from IB discovery to clinical implementation. The current gold-standard for measuring precision of IBs are dedicated double baseline (repeatability) studies Winfield et al. [2017, 2019]. Patients are asked to undergo the same scan twice with an identical patient set-up performed each time, preferably prior to any medical intervention, to ensure that any detected changes characterize the precision of the imaging device. Standard statistical methodologies such as Bland-Altman analysis are then used to characterize measurement precision and subsequently applied in patient investigations to monitor tumour change following treatment once the precision of the measurement is known. A limitation of current approaches to assessing repeatability is that any measured IB,  $x$ , is typically assumed to be a real, univariate or multivariate variable ( $x \in \mathbb{R}$  or  $x \in \mathbb{R}^D$ ). Although this may be justifiable in many cases, it limits the scope of IBs from imaging studies and does not directly apply to monitoring changes in intra-tumoral heterogeneity and habitat maps.

Here we propose a Bayesian paradigm to determine general precision in biomarker studies. In particular, this methodology broadens the scope of IB precision studies to include biomarkers that could be another category of variable. For example, in the case of habitat imaging we hypothesize that IBs are better described by the unit simplex.

In the first section of our paper, we present the theoretical foundation of our approach, structured around four key innovations:

1. **Equivalence to Conventional Methods.** We establish, through theoretical arguments, that this Bayesian approach is equivalent to conventional methods such as Bland-Altman (BA) analysis Bland and Altman [1986] under reasonable assumptions. Importantly, we demonstrate the mathematical equivalence between BA analysis and the broader concept of novelty detection when applied to real-valued biomarkers.

2. **Bayesian Novelty Detection Framework.** We propose a general framework for Bayesian novelty detection applicable to arbitrary response biomarkers. This approach leverages statistical modeling of posterior predictive samples under the null hypothesis of no biomarker change.
3. **Bayesian Metrics for Change Detection.** As an alternative to p-value or novelty estimation, we explore the use of Bayes Factors ( $BF_{10}$ ) and a closely associated equivalent, Posterior Odds ( $PO_{10}$ ), to assess the relative likelihood of biomarker change. Determination of  $PO_{10}$  is achieved through Bayesian mixture modeling, which simultaneously derives posterior distributions of the rate of inter-tumoral response heterogeneity, both at the population and patient levels.
4. **Modeling Intra-Tumoral Heterogeneity.** Finally, we introduce our mathematical model for quantifying intra-tumoral response heterogeneity. The precision of this biomarker is modeled using a Dirichlet-Multinomial (DM) distribution, providing robust statistical insights into intra-tumoral response variability.

To validate the robustness of Hamiltonian Monte Carlo (HMC) in our proposed framework and models, we first conduct comprehensive simulation studies. These simulations model pre- and post-treatment biomarker changes, utilizing both conventional real-valued biomarkers and DM variates representing intra-tumoral heterogeneity. The simulations are performed across a range of plausible biomarker values to ensure their applicability and reliability under realistic conditions.

Finally, we provide a proof-of-concept demonstration of these techniques for assessing heterogeneous responses in metastatic castrate-resistant prostate cancer (mCRPC). Specifically, we use estimates of Apparent Diffusion Coefficient (ADC) from whole-body diffusion-weighted MRI (WBDWI) to compare DM-based biomarkers, which capture intra-tumoral heterogeneity, with conventional median ADC estimates. The documentation of mixed imaging responses to treatment has been highlighted as a key recommendation by the Prostate Cancer Working Group Scher et al. [2016]. This reflects the growing recognition of disease heterogeneity in mCRPC, as well as the coexistence of mixed responses to therapy and overall clinical benefit. WBDWI is emerging as a core imaging biomarker for evaluating therapeutic responses in bone metastases, a critical area where accurate imaging techniques for assessing therapeutic benefit remain limited Blackledge et al. [2014], Padhani et al. [2017]. However, the evaluation of heterogeneous changes in these imaging studies has been challenging to date. Our proposed techniques aim to address this gap by enabling a more nuanced assessment of intra-tumoral response heterogeneity.

## 2 Theory

### 2.1 Introduction to biomarker measurement repeatability

In this article we use the notation  $y_{itk}$  to represent the  $k$ -th biomarker *measurement*, as measured by some medical device, for subject  $i \in \{1, 2, \dots, N\}$  at time  $t \in \{0, 1, \dots, T\}$ . We use  $t = 0$  to indicate that the measurement made before treatment administration (baseline). To simplify notation, if index  $k$  is dropped, this indicates that only a single measurement is available ( $y_{it} \equiv y_{it1}$ ). Furthermore, if index  $i$  is dropped, this indicates a single patient observation ( $y_t \equiv y_{it}$ ). The measurement is assumed to be an estimate of the desired true biomarker of interest  $x_{it}$ , corrupted by bias  $\beta$  and stochastic measurement error  $\sigma$ . The measurement error  $\sigma$  may be due to a number of factors, including inherent noise in the measurement system, inter- and intra-operator variability (e.g. defining the target Region of Interest (ROI) in imaging studies), or patient movement during a scan. Typically, all biomarkers are considered to be single, real-values numbers,  $y \in \mathbb{R}$ , such that:

$$y_{itk} = \beta_0 + \beta_1 x_{it} + \varepsilon_{itk}$$

where  $\varepsilon_{itk}$  is sampled from a zero-mean normal distribution with standard deviation  $\sigma \in \mathbb{R}^+$ , and  $\beta_0$  and  $\beta_1$  represent fixed and proportional bias terms respectively Obuchowski [2018]. Finally, we use  $\alpha_t$  to represent the parameters that describe the population distribution of true biomarker values  $x_t$  at time  $t$ .

A common task in imaging biomarker research is to quantify measurement error,  $\sigma$ , so that it may be accounted for when using biomarkers for patient diagnosis, treatment response evaluation, and population screening O'Connor et al. [2017]. The most popular approach for characterising measurement error is that of Bland and Altman Bland and Altman [1986], which typically relies on access to two or more measurements of the same subject before treatment. Here we use index  $j$  to indicate those patients who have received a double baseline measurement:  $\mathbf{y}_{j0} = (y_{j01}, y_{j02})$  for subject  $j \in \{1, 2, \dots, N_b\}$ . An estimate of measurement error is made using the method of least-squares:

$$\hat{\sigma} = \sqrt{\frac{1}{2N_b} \sum_{j=1}^{N_b} (y_{j02} - y_{j01})^2} \quad (1)$$

which makes assumptions that the expected difference is zero,  $\mathbb{E}\{Y_{02} - Y_{01}\} = 0$ , and that the measurement error is homoskedastic (independent of the biomarker value). It is often useful to verify these assumptions through the Bland-Altman plot, which plots values of  $(y_{j02} - y_{j01})$  against  $(y_{j01} + y_{j02})/2$ . In certain instances it can be advantageous to use the logarithm of the biomarker to improve the assumption of normality and homoscedasticity Euser et al. [2008].

A common use of response biomarkers is to determine whether a treatment causes a significant change in the biomarker value. This is typically assessed by evaluating whether the change in the biomarker measurement at a later time point  $d_i = y_{i1} - y_{i0}$  is sufficiently large to be considered unlikely to arise from measurement error. The Repeatability Coefficient ( $RC$ ), defined as  $RC = 1.96\sqrt{2}\hat{\sigma}$ , provides a symmetric threshold. If  $|d_i| > RC$ , this indicates a significant change in the biomarker, allowing us to reject the null hypothesis ( $H_0 : x_{i0} = x_{i1}$ ) at a significance level of 5%. Additional summary statistics that are reported in repeatability studies include the Intraclass Correlation Coefficient ( $ICC$ ) and Coefficient of Variation ( $CoV$ ) defined as

$$ICC = \frac{\sigma_0^2}{\sigma_0^2 + \sigma^2} \quad CoV = \frac{\sigma}{\mu_0} \times 100\% \quad (2)$$

where  $\mu_0$  and  $\sigma_0$  are parameters that represent the population mean and standard deviation of imaging biomarkers at baseline respectively Bland and Altman [1986], Obuchowski [2018].

A key assumption relevant to the above discussion is that the biomarkers are real-valued and normally distributed, which is somewhat restrictive as biomarkers may not fit this paradigm. For example, with an increase in the efficiency of MR acquisition, many studies now acquire multiple imaging biomarkers in a single sitting, such that they become multidimensional ( $y_{it} \in \mathbb{R}^D$  for  $D > 1$ ) Obuchowski et al. [2023]. Furthermore, biomarkers such as fat fraction and ADC are known to be limited to certain value ranges ( $x_{it} \in [0, 1]$  for fat fraction and  $x_{it} \in [0, 3 \times 10^{-3} \text{ mm}^2/\text{s}]$ ) that may bring the assumption of normally distributed variables into question. Here, we provide an alternative Bayesian framework that might be used to overcome these limitations for use in imaging biomarker research.

## 2.2 Bayesian interpretation of imaging biomarker changes

As illustrated in Figure 1, we consider the problem of detecting a significant change in a given imaging biomarker after treatment as a decision between two competing models for the acquired data: Model  $M_0$  assumes that the true biomarker value at times  $t = 0$  and  $t = 1$  is the same ( $M_0 : x_{i1} = x_{i0}$ ), whilst for Model  $M_1$  this is not the case ( $M_1 : x_{i1} \neq x_{i0}$ ). Both models share parameters  $\alpha_0$ , which describe the distribution of biomarker values at baseline for the population, measurement bias,  $\beta$ , and measurement error,  $\sigma$ . Model  $M_1$  contains an additional set of parameters,  $\alpha_\Delta$ , that describe the distribution of biomarker *changes* across the population. It also permits biomarkers that may be Markovian where  $X_1 \sim p(x_1|x_0, \alpha_\Delta, M_1)$ , though this is not essential. Explicit examples of these parameters are provided in the following sections.

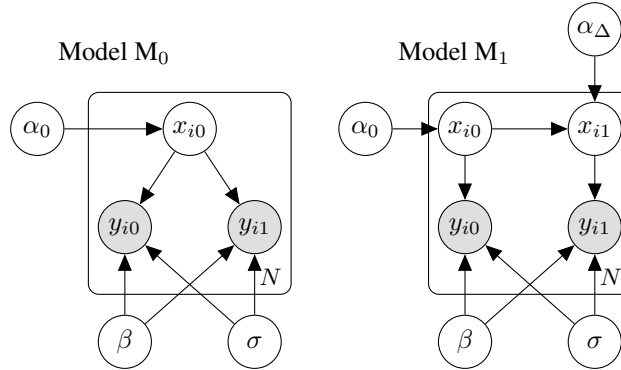


Figure 1: Bayesian networks of two competing models for biomarker measurements made and before,  $y_{i0}$ , and after,  $y_{i1}$ , some intervention for subject  $i$ .

While bias is important in biomarker measurement, it is worth noting here that in the context of measuring post-treatment change, working with biased measurements presents the same fundamental challenge under certain assumptions: If we assume bias to be a generalised function such that  $\beta : x_t \rightarrow x'_t$ , and assume that this function is injective (one-to-one) and invertible, then models  $M_0$  and  $M_1$  may equivalently be represented as  $M_0 : x'_1 = x'_0$  and  $M_1 : x'_1 \neq x'_0$ . In the rest of this article, therefore, we do not distinguish between  $x$  and  $x'$  and use the notation interchangeably and without loss of generality.

Note that although both models only consider pairs of pre- and post-treatment measurements,  $t \in \{0, 1\}$ , some study designs might be interested in biomarker measurements at multiple discrete time intervals,  $t \in \{0, 1, \dots, T\}$ , or indeed in cases with arbitrary time intervals, in which case  $t \in \mathbb{R}^+$ . These use-cases will require further development, but our arguments may also be considered useful in these contexts.

In this paper, we consider two approaches for selecting the model that best explains the observed data. First, we investigate anomaly detection in post-treatment measurements under model  $M_0$  serving as a Bayesian counterpart to null hypothesis testing traditionally used in double-baseline repeatability studies. Second, we explore the use of Bayes Factors ( $BF_{10}$ ) and the closely related Posterior Odds ( $PO_{10}$ ) as methods for directly comparing the likelihoods of the observed data under competing models. We highlight that an advantage of the latter approach is its ability to incorporate prior knowledge about expected changes following treatment into the decision-making process. However, this advantage is accompanied by the added complexity of needing to estimate these expected changes, typically requiring data from clinical trials.

To compare these approaches with classical double baseline methods, we use the case of real, normally-distributed biomarkers as a working example. In this case, the set of baseline parameters are  $\alpha_0 = \{\mu_0, \sigma_0\}$ , and the change parameters  $\alpha_\Delta = \{\mu_\Delta, \sigma_\Delta\}$ , which are fully described in Table 1 along with the assumed data-generating model.

Table 1: Parameters and assumed models for univariate, normally-distributed biomarkers. Note: Half-Cauchy distribution, HC, assumed to have location 0.

Parameter	Description
$\mu_0 \in \mathbb{R}$	Average baseline biomarker value across the population.
$\sigma_0 \in \mathbb{R}^+$	Standard-deviation of baseline biomarker values across the population.
$\mu_\Delta \in \mathbb{R}$	The average change (effect) in the biomarker after treatment.
$\sigma_\Delta \in \mathbb{R}^+$	The standard deviation (heterogeneity) of population biomarker changes.
$\sigma \in \mathbb{R}^+$	The standard deviation of zero-mean normally-distributed noise (measurement uncertainty).
$\sigma_\mu \in \mathbb{R}^+$	Standard deviation of normal prior used when estimating $\mu_0$ and $\mu_\Delta$ .
$\gamma_\sigma \in \mathbb{R}^+$	Scale of the half-Cauchy prior used when estimating $\sigma_0$ , $\sigma_\Delta$ , and $\sigma$ .
Model Distributions	
$\mu_0 \sim \mathcal{N}(0, \sigma_\mu) \quad \mu_\Delta \sim \mathcal{N}(0, \sigma_\mu)$ $\sigma_0 \sim \text{HC}(\gamma_\sigma) \quad \sigma_\Delta \sim \text{HC}(\gamma_\sigma) \quad \sigma \sim \text{HC}(\gamma_\sigma)$ $x_{i0} \sim \mathcal{N}(\mu_0, \sigma_0)$ $x_{i1} \sim \mathcal{N}(x_{i0} + \mu_\Delta, \sigma_\Delta)$ if $M_1$ is true <b>else</b> $x_{i1} = x_{i0}$ $y_{it} \sim \mathcal{N}(x_{it}, \sigma)$	
where	$\mathcal{N}(x; a, b) = (2\pi b^2)^{-1/2} \exp\{-(x - a)^2 / 2b^2\}$ $\text{HC}(x; \gamma_\sigma) = 2 \left[ 1 + (x/\gamma_\sigma)^2 \right] / (\pi\gamma_\sigma), \quad x \geq 0$

### 2.3 Assessing change through anomaly detection

Conventional assessment of response biomarkers for individual patients follows the paradigm of anomaly detection. In the framework presented above this generally involves estimation of the parameters in model  $M_0$ , and then determining whether a change observed after treatment would represent a significant anomaly if model  $M_0$  still holds. This is summarized by a *p-value*, which represents the probability of observing the post-treatment measurement—or a measurement as “extreme” as the post-treatment measurement—under the null hypothesis that no real change has occurred (i.e.  $M_0$  is true). Formerly, we wish to evaluate

$$p = \Pr(T(y) \geq T(y_1) \mid y_0, \mathbf{y}_b, M_0) \quad (3)$$

where  $\mathbf{y}_b$  represent the repeat baseline measurements used to determine the parameters of  $M_0$ , and  $T(\cdot)$  represents some test statistic on observed data that describes how unlikely observed post-treatment data are if  $M_0$  is true. Exact calculation of equation 3 requires knowledge of the marginal distribution of  $y$  conditional on all observed data

$$p(y|y_0, \mathbf{y}_b, M_0) = \int_{\alpha_0} \int_{\sigma} p(y|y_0, \alpha_0, \sigma, M_0) p(\alpha_0|y_0, \mathbf{y}_b, M_0) p(\sigma|\mathbf{y}_b, M_0) d\alpha_0 d\sigma \quad (4)$$

In all but a handful of cases, it is generally not possible to directly evaluate this integral. In the following two subsections we demonstrate how conventional repeatability analysis may be considered a special case of this formulation, and then discuss how numerical techniques can be used to solve this problem in a general setting.

### 2.3.1 Analytical solutions

In the working example of normally distributed biomarkers with  $\alpha_0 = (\mu_0, \sigma_0)$  the convention is to assume that these parameters, along with error  $\sigma$ , are known *a-priori* (estimated from double baseline data for example). In the Supplementary Material, theorem 7.1 we prove that under these assumptions, the following conditional probability is true.

$$p(y|y_0, \sigma, \mu_0, \sigma_0, M_0) = \mathcal{N}(y; \mu^*, \sigma^*) \quad (5)$$

where

$$\mu^* = ICC \cdot y_0 + (1 - ICC) \cdot \mu_0 \quad \sigma^* = \sqrt{1 + ICC} \cdot \sigma$$

If the variance of baseline biomarker values amongst the population is much larger than the measurement uncertainty ( $\sigma_0 \gg \sigma$ ) such that  $ICC \rightarrow 1$ , then we obtain the classical result  $p(y|y_0, \sigma, M_0) = \mathcal{N}(y; y_0, \sqrt{2}\sigma)$ . This may be re-written as  $p(d|\sigma, M_0) = \mathcal{N}(d; 0, \sqrt{2}\sigma)$  where  $d = y - y_0$ . When determining whether a change following treatment is significant, the test static is the  $z$ -statistic,  $z = (y_1 - y_0)/\sqrt{2}\sigma$ , such that for  $p < 0.05$  in a two-sided hypothesis test we require  $|d| > 1.96\sqrt{2}\sigma = RC$  as discussed earlier (Section 2.1).

Although simpler derivations of this final result are possible, equation 5 provides a transparent formulation; it demonstrates a key assumption made throughout conventional repeatability analysis that  $ICC \rightarrow 1$  indicating that significant changes after treatment are independent of baseline value. This may be a poor assumption to make. For example, in the case of changes in ADC in bone cancer, a change from 0.8 to  $1.5 \times 10^{-3}$  s/mm<sup>2</sup> might have a different biological interpretation (reduction in tumour cellularity) than a change from 0.3 to  $1.0 \times 10^{-3}$  s/mm<sup>2</sup> (a potential region of new disease in an area of displaced yellow marrow). The  $ICC$ , along with  $\mu_0$ , provide some context to these changes as they describe the distribution of expected baseline measurements for a patient cohort.

As a corollary, if we continue with the assumption that  $ICC \rightarrow 1$  it is also relatively straightforward to marginalize over the uncertainty of  $\sigma$  and obtain the precise form of equation 4 (see Supplementary Material, corollary 7.1.1):

$$p(y|y_0, \mathbf{y}_b, M_0) = \frac{\Gamma\left(\frac{N_b+1}{2}\right)}{\sqrt{\pi N_b} \Gamma\left(\frac{N_b}{2}\right)} \left(1 + \frac{t^2}{N_b}\right)^{-\frac{N_b+1}{2}}$$

where

$$t = \frac{y - y_0}{\sqrt{\frac{1}{N_b} \sum_i (y_{j02} - y_{j01})^2}} = \frac{d}{\sqrt{2}\hat{\sigma}}$$

Specifically,  $p(y|y_0, \mathbf{y}_b, M_0)$  follows a Student- $t$  distribution with  $N_b$  degrees of freedom. Significant change following treatment is determined by assessing whether  $t$  exceeds a threshold defined by the Student- $t$  distribution at the chosen significance level. This corresponds to the condition  $|d| > \gamma\sqrt{2}\hat{\sigma}$  where  $\gamma$  is a factor dependent on  $N_b$  and the specified significance level. Notably,  $\gamma \rightarrow 1.96$  as  $N_b \rightarrow \infty$  for  $p = 0.05$ .

### 2.3.2 Numerical solutions

Although exact marginalization of parameters  $\alpha_0$  and  $\sigma$  in equation 4 is generally not possible, it can be achieved numerically through Markov-Chain Monte-Carlo (MCMC) sampling techniques. Using this approach we draw samples,  $s \in \{1, 2, \dots, M_s\}$ , of the parameters of interest from their conditional posterior distribution,  $\alpha_0^s, x_0^s, \sigma^s \sim p(\alpha_0, x_0, \sigma | \alpha_0^{s-1}, x_0^{s-1}, \sigma^{s-1}, y_0, \mathbf{y}_b)$ , and subsequently draw posterior predictive data samples from the assumed likelihood distribution for model  $M_0$ ,  $y^s \sim p(y | x_0^s, \sigma^s, M_0)$ ; the complete set of  $y^s$  are then samples from the marginalised distribution:  $p(y|y_0, \mathbf{y}_b, M_0)$ .

#### Pseudocode

```

 $\alpha_0^0, x_0^0, \sigma^0$  = Initial parameter estimates
 $N_s$  = number of samples
for  $s \in \{1, 2, \dots, N_s\}$  do
     $\alpha_0^s \sim p(\alpha_0 | \alpha_0^{s-1}, x_0^{s-1}, \sigma^{s-1}, y_0, \mathbf{y}_b)$ 
     $x_0^s \sim p(x_0 | \alpha_0^s, x_0^{s-1}, \sigma^{s-1}, y_0, \mathbf{y}_b)$ 
     $\sigma^s \sim p(\sigma | \alpha_0^s, x_0^s, \sigma^{s-1}, y_0, \mathbf{y}_b)$ 
    
```

```

         $y^s \sim p(y|x_0^s, \sigma, M_0)$ 
    end for
    return  $\mathbf{y}^s = \{y^1, \dots, y^{N_s}\}$ 
    
```

Initial parameter estimates  $\alpha_0$ ,  $x_0$ , and  $\sigma_0$  are highly model-dependent but can, for instance, be obtained using maximum likelihood estimation to improve convergence speed. It is standard practice to discard or “burn” an initial portion of the samples to minimize the influence of the starting conditions on subsequent samples. Additionally, samples are typically generated across two or more independent chains to ensure that the model sampling has converged—meaning the chains appear to sample parameters from the same underlying distribution. When multiple chains are used, the Gelman-Rubin statistic  $\hat{R}$  can be employed to assess convergence. A value of  $\hat{R}$  close to 1 indicates that the chains have converged well Gelman and Rubin [1992].

Novelty detection using MCMC sampling is more involved than for the analytical solutions presented above. It may involve analysis of biomarkers other than real variables, or involve probability distributions other than the univariate/multivariate normal distributions. Our approach is to approximate the posterior predictive distribution (equation4) as some suitable density estimation derived from the posterior predictive samples  $\mathbf{y}^s$

$$p(y|y_0, \mathbf{y}_b, M_0) \approx \hat{p}_s(y|\mathbf{y}^s)$$

Density approximation  $\hat{p}_s$  might be based on kernel density estimation or, as we employ, a relevant finite mixture model. By estimating the maximum location of the posterior predictive distribution

$$y^\dagger = \arg \max_y [\hat{p}_s(y|\mathbf{y}^s)]$$

we define the “kernel distance”,  $D(y) \in \mathbb{R}^+$ :

$$D(y) = |\hat{p}_s(y^\dagger|\mathbf{y}^s) - \hat{p}_s(y|\mathbf{y}^s)|$$

Computing this distance for all samples generated via the MCMC algorithm,  $D(\mathbf{y}^s)$ , the credible region is the set of all  $y$  for which  $D(y) > (1 - \alpha)^{\text{th}}$  percentile of  $D(\mathbf{y}^s)$ , where  $\alpha$  represents some desired significance level (e.g.  $\alpha = 0.05$ ). Any post-treatment measurement,  $y_1$ , that lies outside this region is then considered to be an anomaly. An example of an estimated credible region defined for synthetic data simulated from a multivariate normal distribution is illustrated in Figure 2.

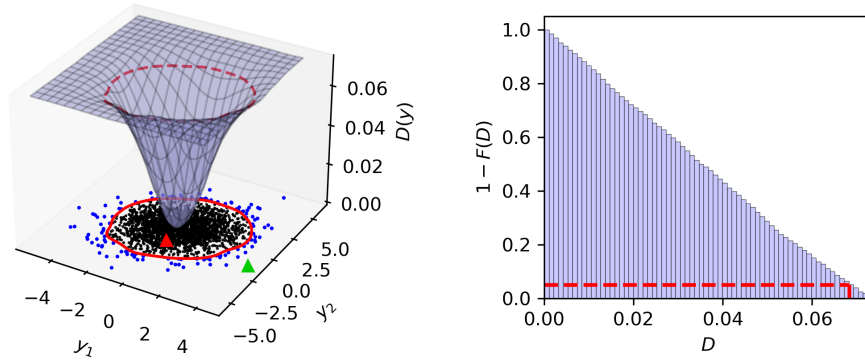


Figure 2: Example 95% credible region (red contour) for 5000 samples from a 2-dimensional normal distribution, computed using the kernel distance,  $D$  (blue surface). MCMC samples that are found to be outside the credible regions are color-coded blue, whilst those inside are color-coded black. Triangles represent example data from a post-treatment measurement; the green triangle shows a case that would be considered a significant change compared to baseline, whilst the red triangle illustrates a case for which there is insufficient evidence for a significant change. In this example, we use an isotropic Gaussian kernel with bandwidth  $h = 0.5$  to generate kernel density estimate.

## 2.4 Bayes factors

As an alternative to novelty detection, the Bayes factor compares the evidence in favour of both models  $M_0$  and  $M_1$  by calculating the ratio of the marginal likelihoods of the observed data,  $\mathbf{y}$ :

$$BF_{10} = \frac{p(\mathbf{y}|M_1)}{p(\mathbf{y}|M_0)} = \frac{\int_{\alpha_1} p(\mathbf{y}|\alpha_1, M_1)p(\alpha_1)d\alpha_1}{\int_{\alpha_0} p(\mathbf{y}|\alpha_0, M_0)p(\alpha_0)d\alpha_0} \quad (6)$$

for  $BF_{10} \in \mathbb{R}^+$  Gronau et al. [2017]. A theoretical advantage of the Bayes factor is that it allows one to both reject the null model,  $M_0$ , in favour of  $M_1$  when  $BF_{10} > 1$  or confirm its existence when  $BF_{10} < 1$ . Moreover, if  $BF_{10} \approx 1$  to within some appropriate tolerance, this indicates that inadequate data is present to choose between either model. As when using p-values during statistical significance testing, there are no fixed rules when using Bayes factors to interpret results of some experiment; the final decision should depend on the context in which the experiment was performed and might be influenced by supplementary information. Our aim in this article is to outline methods for estimating the Bayes factor within repeatability studies as a tool to aid measurement of the magnitude of change in biomarkers following treatment. Whether this change reaches some threshold to warrant any clinical decision should always include other factors such as patient history, bloods markers, treatment selection, and expected patient benefit. That said, several experts have suggested approximate schemes for decision-making based on Bayes factors, including a framework by Lee and Wagenmakers, as summarized in Table 2 Lee and Wagenmakers [2014].

Table 2: Interpretation thresholds for Bayes factors suggested by Jeffreys

$BF_{10}$	Interpretation
$> 30$	Very strong evidence for $M_1$ compared to $M_0$
10–30	Strong evidence for $M_1$ compared to $M_0$
3–10	Moderate evidence for $M_1$ compared to $M_0$
1–3	Anecdotal evidence for $M_1$ compared to $M_0$
$\frac{1}{3} - 1$	Anecdotal evidence for $M_0$ compared to $M_1$
$\frac{1}{10} - \frac{1}{3}$	Moderate evidence for $M_0$ compared to $M_1$
$< \frac{1}{10}$	Strong evidence for $M_0$ compared to $M_1$

#### 2.4.1 Analytical solutions

For our working example of real-value normally-distributed measurements (table 1), it is possible to derive a formula for the Bayes factor for the measured change in a single patient,  $d_y = y_1 - y_0$ , provided the parameters for both models are known. In the Supplementary Material, theorem 7.2, we demonstrate that the natural logarithm of the Bayes factor in this instance is given by

$$\ln(BF_{10}) = \frac{1}{2} \left( \ln(1 - \eta) - (1 - \eta) \left( \frac{d_y - \mu_\Delta}{\sqrt{2}\sigma} \right)^2 + \left( \frac{d_y}{\sqrt{2}\sigma} \right)^2 \right) \quad (7)$$

where

$$\eta = \frac{\sigma_\Delta^2}{\sigma_\Delta^2 + 2\sigma^2}$$

encapsulates the magnitude of the heterogeneity of biomarker changes following treatment,  $\sigma_\Delta$ , in terms of measurement uncertainty (described as the Inter Measurement Sensitivity (*IMS*) in Thrussell et al. [2022]). Some intuition of the Bayes factor can be made by investigating the functional form of its expectation when model  $M_0$  is true or when model  $M_1$  is true (see Supplementary Material, corollary 7.2.1 for the derivation):

$$\begin{aligned} \mathbb{E}_{d_y|M_0} \{\ln(BF_{10})\} &= \frac{1}{2} (\ln(1 - \eta) + \eta - (1 - \eta)\xi^2) \\ \mathbb{E}_{d_y|M_1} \{\ln(BF_{10})\} &= \frac{1}{2} \left( \ln(1 - \eta) + \frac{\eta}{1 - \eta} + \xi^2 \right) \end{aligned}$$

where  $\xi = |\mu_\Delta|/\sqrt{2}\sigma$  represents the *effect size* of the treatment. Plots of these functions are illustrated in Figure 3 for different values of  $\eta$  and  $\xi$ . There is a clear trend that as  $\eta$  and  $\xi$  increase, the expectation of the Bayes factor when model  $M_1$  is true increases, indicating better sensitivity for detecting post-treatment change. Similarly, increasing  $\xi$  reduces the expectation value when model  $M_0$  is true indicating improved specificity for confirming no-change. However, it is interesting that for moderate effect sizes this specificity is lost as the heterogeneity of treatment change increases ( $\eta \rightarrow 1$ ).

#### 2.5 Numerical solutions with Bayesian mixture modelling

In the results presented in the preceding section we made the assumption that model  $M_1$  parameters,  $\alpha_1 = (\sigma_\Delta, \mu_\Delta)$  are known. Unfortunately, unlike for  $M_0$  and parameters  $\alpha_0$  where double baseline experiments can be specifically

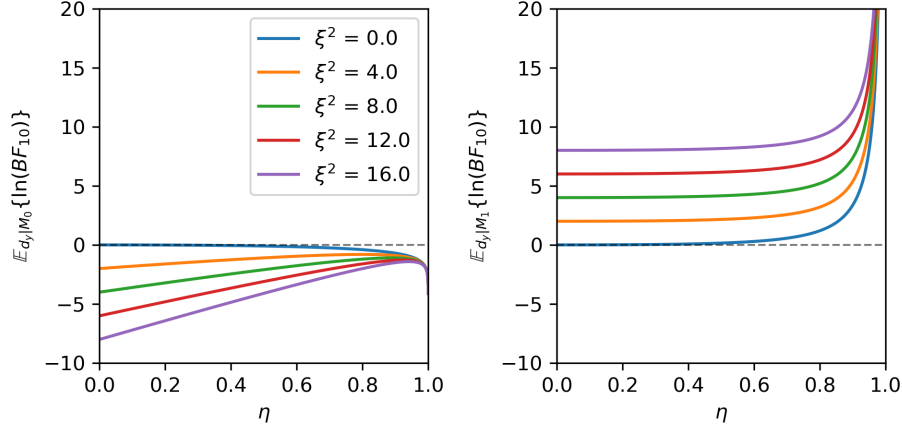


Figure 3: Variation in the expected Bayes factor for real, normally-distributed biomarker measurements.

constructed such that the relevant model assumptions are somewhat guaranteed, it is difficult to acquire data that provide direct estimation of  $\alpha_1$ . In a clinical trial setting, for example, this would require knowledge of the response label for each patient,  $z_i \in \{M_0, M_1\}$ . This could, for example, be derived from other criteria such as patient overall survival, progression-free survival, or even subjective radiologist assessment of all available patient data. However, in many cancer trials medical imaging is used as a key criteria for early response assessment and so joint estimation of model labels  $z_i$  and model parameters would be preferable. Here we propose that Bayesian mixture modelling may be used to achieve this and subsequently estimate Bayes factors for each subject within a trial.

Consider a trial consisting of  $N$  subjects, where biomarker measurements are made for each subject before and after treatment,  $\mathbf{y} = \{y_{i0}, y_{i1}\}$  for  $i \in \{1, \dots, N\}$ . Furthermore, assume that double baseline measurements,  $\mathbf{y}_{j0} = \{y_{j01}, y_{j02}\}$  are available for  $j \in \{1, \dots, N_b\}$ . These data - whether belonging to the same group, a subset, or an entirely different cohort than the main trial - should be representative of the biomarker measurements made within the main study, and acquired in such a way that ensures the assumption of model  $M_0$  holds. The prior probability of each model is now incorporated as an unknown parameter  $\lambda \in (0, 1)$  such that  $p(z_i = M_1) = \lambda$  and  $p(z_i = M_0) = 1 - \lambda$ . The posterior distribution of all model parameters, marginalised over the unknown data labels is:

$$\begin{aligned}
 p(\alpha_0, \alpha_1, \sigma, \lambda, \mathbf{x}, \mathbf{x}_b | \mathbf{y}, \mathbf{y}_b) &\propto \\
 p(\alpha_0) p(\alpha_1) p(\sigma) &\prod_{j=1}^{N_b} p(y_{bj1} | x_{bj}, \sigma) p(y_{bj2} | x_{bj}, \sigma) p(x_{bj} | \alpha_0) \\
 &\times \prod_{i=1}^N p(y_{i0} | x_{i0}, \sigma) p(x_{i0} | \alpha_0) \{ \lambda \cdot p(y_{i1} | x_{i1}, \sigma) p(x_{i1} | x_{i0}, \alpha_1) \\
 &\quad + (1 - \lambda) \cdot p(y_{i1} | x_{i0}, \sigma) \}
 \end{aligned} \tag{8}$$

where  $p(\alpha_0)$ ,  $p(\alpha_1)$ , and  $p(\sigma)$  represent suitably chosen prior distribution on model parameters, and  $\mathbf{x}$  and  $\mathbf{x}_b$  represent the true (unknown) biomarker values from which measurements  $\mathbf{y}$  and  $\mathbf{y}_b$  have been acquired. Samples from this posterior distribution may be directly sampled using Bayesian inference engines such as Stan, which provides a sequence of samples  $s \in \{1, 2, \dots, N_s\}$  of model parameters  $(\alpha_0^s, \alpha_1^s, \sigma^s, \lambda^s, \mathbf{x}^s, \mathbf{x}^{bs})$ .

Directly obtaining Bayes factors using this approach is complicated by not knowing the prior probability of either model,  $p(M_0)$  or  $p(M_1)$ . We therefore use a related quantity, the Posterior Odds ( $PO_{10}$ ), defined as

$$PO_{10} = \frac{p(z_i = M_1 | y_{i0}, y_{i1})}{p(z_i = M_0 | y_{i0}, y_{i1})}$$

which is equivalent to the Bayes factor when  $P(M_0) = P(M_1)$ . Although the posterior distribution for each patient label  $p(z_i = M_k | y_{i0}, y_{i1})$  is not known, samples from this distribution can be obtained during the MCMC process by sampling from a categorical distribution, conditional on all model parameters:

$$z^s \sim \begin{cases} M_0, & \text{with probability } p_0^s \\ M_1, & \text{with probability } 1 - p_0^s \end{cases}$$

where

$$p_0^s = \frac{\tilde{p}_0^s}{\tilde{p}_0^s + \tilde{p}_1^s}$$

and

$$\begin{aligned}\tilde{p}_0^s &= p(y_{i0}|x_{i0}^s, \sigma^s)p(y_{i1}|x_{i0}^s, \sigma^s)(1 - \lambda^s) \\ \tilde{p}_1^s &= p(y_{i0}|x_{i0}^s, \sigma^s)p(y_{i1}|x_{i1}^s, \sigma^s)\lambda^s\end{aligned}$$

Finally, we estimate the posterior odds by:

$$PO_{10} = \frac{\hat{p}(z_i = M_1|y_{i0}, y_{i1})}{\hat{p}(z_i = M_0|y_{i0}, y_{i1})} = \frac{\frac{1}{N_s} \sum_s (z_i^s == M_1)}{\frac{1}{N_s} \sum_s (z_i^s == M_0)}$$

## 2.6 Application to habitat mapping

In this article we demonstrate a use-case of the methods presented above in monitoring heterogeneous change in tumours. There are many approaches for quantifying intra-tumoral heterogeneity in cancer. This may include techniques like radiomics, which attempt to derive hand-crafted or deep features from images that are designed to represent apparent texture within the images. This approach quantifies heterogeneity within images to a set of (hopefully) independent univariate biomarkers, for which conventional repeatability assessments are useful. However, radiomics features generally ignore the spatial context, since the extracted features represent the entire image or tumor. An alternative is “habitat imaging”, which attempts to automatically classify subregions within the tumour that ideally represent distinct biological phenotypes. The methods for defining such maps are numerous, but in general they lead to a biomarker that may be considered to be the proportion of tumour in each of  $M$  possible tissue categories. That is  $x = \{x_1, \dots, x_M\}$  is a simplex with the property that  $\sum_m x_m = 1$ , and  $x_m$  is the proportion of tissue belong to class  $m$ . As far as we are aware, no method of repeatability evaluation for such biomarkers is available.

Our approach to obtaining response habitats is illustrated in Figure 4, inspired from the work of previous publications Koh et al. [2009], Blackledge et al. [2017], Dalili et al. [2017]. Considering each tumour individually, we derive the 10<sup>th</sup> and 90<sup>th</sup> percentiles of the ADC distribution from baseline measurements, leading to  $M = 3$  distinct ADC regions. The number of ADC voxels within these regions in the tumour after treatment constitute our biomarker measurement of interest,  $y_1 \in \mathbb{Z}^3$ . It is important to note that we do not directly normalize the measurement,  $y_{1m} \rightarrow y_{1m} / \sum_m y_{1m}$ , as this leads to numerical instability wherever there are no voxels within a particular ADC range (can occur for small tumours). Visualization of these biomarker measurements, however, is performed following normalization to improve interpretation.

Whether a particular value of  $y_1$  constitutes a significant change following treatment can be determined using our theoretical framework and the availability of some double-baseline data  $y_b$ . A key assumption in our model is that  $x_0$  is a known quantity, as it has been defined by setting the percentile values for the baseline distribution,  $x_0 = \mu_0 = (0.1, 0.8, 0.1)$ . Additional parameters, along with the data generating model, are presented in Table 3

## 3 Materials and Methods

### 3.1 Simulation Studies

Data were simulated for both median ADC and habitat models (tables 1 and 3 respectively) based on the parameter values and ranges outlined in tables 4 and 5. For parameters specified as ranges, Latin hypercube sampling was employed to generate five hundred unique combinations of these parameters, ensuring a thorough exploration of the parameter space. For each parameter combination, data were sampled 20 times, and the models were fit using Stan with the code provided in Supplementary Information Sections 7.3 and 7.4. For habitat data generation, the number of voxels associated with each datum was sampled from a log-normal distribution characterized by a mean ( $\mu_v$ ) and standard deviation ( $\sigma_v$ ), derived from voxel size estimates observed in the clinical studies.

For each data sample and parameter combination, we evaluated the following diagnostics:

- **Bias:** The bias for each parameter was calculated as  $((y_{med} - y_{true}) / y_{true}) \times 100\%$ , where  $y_{true}$  is the true parameter, and  $y_{med}$  is the median of the posterior samples for that parameter.
- **Coverage:** The coverage was defined as the percentage of cases in which the true parameter value fell within the 95% credible interval of the posterior samples.

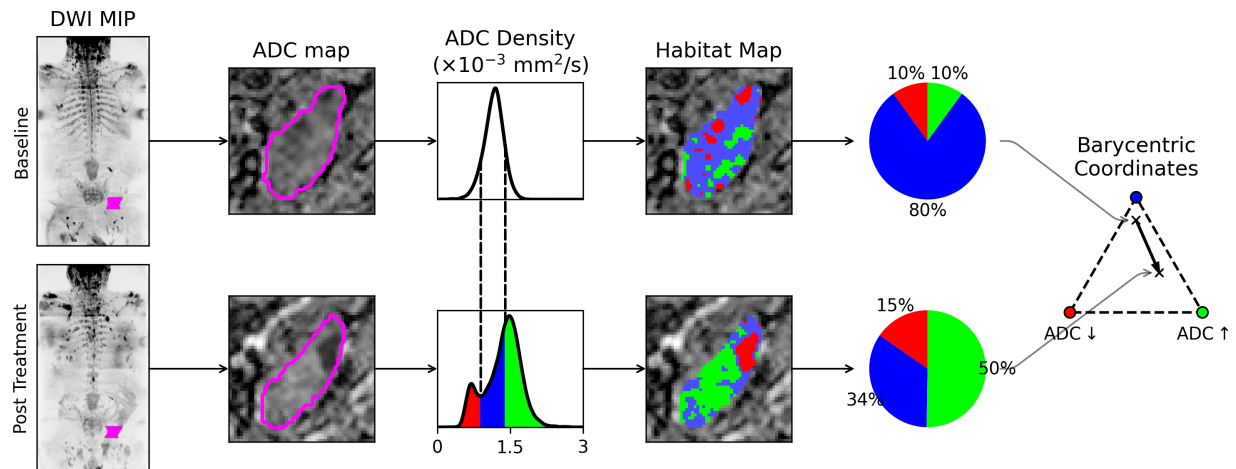


Figure 4: Our approach to habitat mapping for post-treatment assessment consists (from left to right) of: (i) Delineating Regions of Interest (ROIs) around individual lesions on clinical imaging (represented here as a pink overlay on the high b-value Maximum Intensity Projection (MIP)). (ii) Transferring these contours to the derived ADC maps. (iii) Deriving ADC percentiles from the baseline distribution and applying them to the follow-up scan to derive regions within the percentile ranges. (iv) Visualizing the location of responding regions as green where ADC has increased, and progressing regions as red where ADC has decreased. (v) Identifying the proportions of like habitat voxels as a pie-chart to represent the simplex, or (vi) using barycentric coordinates to monitor how the derived simplexes change following treatment.

Table 3: Parameters and assumed models for unnormalised simplex (habitat) biomarkers. Note: Half-Cauchy distribution, HC, assumed to have location 0.

Parameter	Description
$\mu_0 \in \mathbb{R}^M$	The assumed baseline habitat values. Here equal to (0.1, 0.8, 0.1).
$\mu_1 \in \mathbb{R}^M$	The center (average) of post-treatment values.
$\tau \in \mathbb{R}^+$	Precision of baseline measurements.
$\tau_1 \in \mathbb{R}^+$	Concentration of population post-treatment values.
$N_v \in \mathbb{Z}^+$	Number of tumour voxels ( $\sum_m y_m = N_v$ ).
$\gamma_\tau \in \mathbb{R}^+$	Scale of the half-Cauchy prior used when estimating $\tau$ and $\tau_1$ .
Model Distributions	
$\tau \sim \text{HC}(\gamma_\tau)$ $x_{i1} \sim \text{Dir}(\mu_1, \tau_1)$ if $M_1$ is true else $x_{i1} \sim \text{Dir}(\mu_0, \tau)$ $y_{i1} \sim \text{Mult}(x_{i1}, N_v)$	
where	$\text{Dir}(x; \mu, \tau) = \frac{\Gamma(\tau)}{\prod_m \Gamma(\tau \mu_m)} \prod_{m=1}^M x_m^{\tau \mu_m - 1}$ $\text{Mult}(y; x, N_v) = \frac{N_v!}{y_1! \dots y_M!} x_1^{y_1} \dots x_M^{y_M}$ $\text{HC}(x; \gamma_\tau) = 2 \left[ 1 + (x/\gamma_\tau)^2 \right] / (\pi \gamma_\tau)$

- $\hat{R}$  (**Gelman-Rubin Diagnostic**): The Gelman-Rubin diagnostic Gelman and Rubin [1992] was estimated using the ArviZ package Kumar et al. [2019] to assess the convergence of the HMC chains.
- **Diagnostic Accuracy**: For each parameter combination, the diagnostic accuracy of the posterior odds estimate was quantified through sensitivity, specificity, and the area under the receiver operating characteristic (ROC) curve (AUC). The true label of change/no change was sampled as  $l = \text{Uniform}(0, 1) < \lambda$ .

Table 4: Parameter values and ranges for median ADC simulations.

Parameter	Value/Range
Mixing proportion, $\lambda$	0.4 $\rightarrow$ 0.95
IMS, $\eta = \sigma_{\Delta}^2 / (\sigma_{\Delta}^2 + 2\sigma^2)$	0.6 $\rightarrow$ 0.99
ICC = $\sigma_0^2 / (\sigma_0^2 + \sigma^2)$	0.6 $\rightarrow$ 0.99
Mean change, $\mu_{\Delta}$	$-0.5 \rightarrow 2.0 \times 10^{-3} \text{ mm}^2/\text{s}$
Baseline mean, $\mu_0$	$1.0 \times 10^{-3} \text{ mm}^2/\text{s}$
Measurement variation, $\sigma$	$0.05 \times 10^{-3} \text{ mm}^2/\text{s}$

Table 5: Parameter values and ranges for habitat simulations.

Parameter	Value/Range
Mixing proportion, $\lambda$	0.4 $\rightarrow$ 0.95
IMS, $\eta = \tau / (\tau + \tau_1)$	0.6 $\rightarrow$ 0.99
Baseline value, $\mu_0$	(0.1, 0.8, 0.1)
Post-treatment center, $\mu_1$	(0.01, 0.54, 0.36)
Measurement precision, $\tau$	11.54
Voxel size mean, $\mu_v$	6.37
Voxel size std-dev, $\sigma_v$	1.38

### 3.2 Patient cohort and image acquisition

All WBDWI data were acquired at a single institution as part of three independent imaging studies. These studies were approved by the local research and ethics committee, and all patients were recruited and consented at a single institution. Inclusion criteria were: histopathological diagnosis of prostate cancer, history of bone metastases and no contraindication for MRI acquisition.

**Study 1** investigated the use of ADC derived from WBDWI to assess the response of Radium-223 as a therapeutic agent in 35 patients diagnosed with metastatic castrate-resistant prostate cancer (mCRPC). Images were acquired before and after treatment with a median time between scans of 28 days (range: 21–35 days) using a protocol that consisted of either two b-values ( $b = 50$  and  $800\text{s}/\text{mm}^2$  in two patients or  $50$  and  $900\text{s}/\text{mm}^2$  in one other), or three b-values ( $b = 50, 600,$  and  $900\text{s}/\text{mm}^2$  in all other patients). All images were acquired on a 1.5T system, using a 2D twice-refocused spin-echo echo-planar imaging (EPI) sequence, with trace-weighted diffusion encoding and inversion-recovery fat suppression. Images were acquired over 3–5 imaging stations, comprising 40 slices/station in the axial plane over 128 columns (left–right/readout direction) and 96–116 rows (anterior–superior/phase–encode direction). Scanner-based interpolation was used to double the isotropic in–plane image resolution to  $1.7\text{mm}^2$  and a slice thickness of 5mm.

**Study 2** investigated the use of ADC derived from WBDWI to assess the response of a chemotherapeutic agent in 14 patients diagnosed with mCRPC. Images were acquired before and after treatment with a median time between scans of 84 days (range: 42–173 days) using a protocol that consisted of three b-values ( $b = 50, 600,$  and  $900\text{s}/\text{mm}^2$ ). All images were acquired on a 1.5T system, using a 2D twice-refocused spin-echo echo-planar imaging (EPI) sequence, with trace-weighted diffusion encoding and inversion-recovery fat suppression. Images were acquired over 3–5 imaging stations, comprising 40 or 50 slices/station in the axial plane over 128 or 150 columns (left–right/readout direction) and 124 or 144 rows (anterior–superior/phase–encode direction). Scanner-based interpolation was used to double the isotropic in–plane image resolution to 1.3, 1.4, or  $1.5\text{mm}^2$  and a slice thickness of 5mm.

**Study 3** was a double baseline study comprising 10 patients diagnosed with mCRPC, scanned prior to treatment. All patients were scanned twice on the same day, with repositioning between the examinations. Diffusion-weighted imaging consisted of three b-values ( $b = 50, 600,$  and  $900\text{s}/\text{mm}^2$ ), acquired on a 1.5T system using a 2D twice-refocused spin-echo echo-planar imaging (EPI) sequence, using trace-weighted diffusion encoding and inversion–recovery fat suppression. Images were acquired over 3 or 4 imaging stations, comprising 42 slices/station in the axial plane over 128 columns (left–right/readout direction) and 104 or 128 rows (anterior–superior/phase–encode direction). Scanner-based interpolation was used to double the isotropic in–plane image resolution to  $1.7\text{mm}^2$  and a slice thickness of 6mm.

### 3.3 Image and data processing

Using the OsiriX Dicom viewing platform Rosset et al. [2004], a radiologist with over five years of experience in body MRI for cancer, manually delineated up to six target lesions in each patient on the low b-value images, using available anatomical imaging (e.g. Dixon or T2-weighted) to assist in target definition. They ensured that the same lesion was

visible at both time-points for each study, so that they may be monitored over time. This resulted in a total of 120, 68, and 73 lesions delineated for Study 1, Study 2, and Study 3 respectively. The median lesion volumes were (at baseline) 12.5ml (inter-quartile range (IQR): 4.2–31.7ml), 22.0ml (9.0–35.9ml), and 5.1ml (2.0–9.2ml) for studies 1, 2, and 3 respectively. A dedicated script was developed using the pyOsiriX plugin Blackledge et al. [2016] that calculated maps of ADC using maximum-likelihood estimation and incorporating all available b-values for each study.

For each lesion, median ADC values within each lesion were recorded. Furthermore, habitat maps were calculated according to the methods described in section 2.6, using baseline ADC percentile thresholds of 10% and 90%. We subsequently used the Stan programming language to fit our proposed mixture models for each marker as defined in section 2.6 for **Study 1** and **Study 2** independently (code provided in Supplementary Material 7.3 and 7.4). In both cases data from **Study 3** were used as the double baseline images. Posterior predictive samples were obtained so that we could investigate our proposed numerical approach to anomaly detection. The posterior density of these samples was approximated using a 5-component Dirichlet mixture model using an in-house expectation maximization routine. The position with maximum posterior density was subsequently found using a Nelder-Mead optimization routine, with a coarse grid-search used for initialization. This allowed us to determine the credible region, using the method outlined in section 2.3.2. Furthermore, model label samples were generated in order to test our approach to posterior odds calculation (section 2.5)]. For each model fit, we used 3 independent MCMC chains, each consisting of 5000 samples (following a burn-in period of 500 samples). We did not perform any sample thinning, leading to a total of 15000 samples per parameter. Sample convergence was determined using the Gelman-Rubin statistic,  $\hat{R}$ , Gelman and Rubin [1992] using the ArviZ package Kumar et al. [2019].

## 4 Results

### 4.1 Simulation Studies

Figure 5 presents the simulation results for our median ADC model. Overall, the parameter estimates appear to be unbiased, with credible intervals derived from posterior samples demonstrating good coverage for all sampled parameter values. However, a notable exception occurs in scenarios where  $|\mu_\Delta| \rightarrow 0$  and  $\eta \rightarrow 0.5$ . In these cases, the model struggles to distinguish between post-treatment change and no change, as the models for change and no-change become increasingly similar. This challenge is also reflected in the accuracy diagnostics, which are particularly poor in this parameter region. Notably, in certain parameter ranges, the posterior odds-based model comparison achieves 100% sensitivity and 100% specificity. This performance starkly contrasts with the use of p-values, which are theoretically limited to a maximum specificity of 95% by design.

Figure 6 presents the simulation results for our habitat model. Overall, there appears to be minimal bias across the range of parameters investigated, with the posterior credible intervals effectively capturing the true values. In terms of accuracy diagnostics, the habitat model demonstrates improved area AUC and sensitivity compared to the median ADC model. However, this improvement comes at the cost of reduced specificity in certain parameter ranges. A general decline in metric performance is observed as the proportion of regions exhibiting change decreases ( $\lambda \rightarrow 0.4$ ), reflecting fewer samples representing change. Additionally, a drop in performance is evident as the IMS decreases ( $\eta \rightarrow 0.6$ ), further challenging the model’s ability to distinguish between change and no-change scenarios.

### 4.2 Patient Studies

In figure 7 we present 5 patient example cases, two from study 1 and three from study 2. In each case we present summaries of each of the target lesions, including their derived habitat map (central slice only), and their location on the high b-value MIP. We color-code the lesion on the MIP according to the value of the estimated posterior odds, which is binned into one of five possible categories:  $PO_{10} \leq \frac{1}{3}$  (maroon) indicating moderate evidence of no change,  $\frac{1}{3} < PO_{10} \leq 3$  (orange) indicating insufficient evidence to say whether a lesion demonstrates significant change,  $3 < PO_{10} \leq 10$  (yellow) indicating moderate evidence of significant change,  $10 < PO_{10} \leq 30$  (teal) and  $BF_{10} > 10$  (dark green) indicating strong and very strong evidence of change respectively. These colors are all used to plot the changes in habitats in barycentric coordinates, along with the credible region shown as a grey area (for novelty detection). One observation is that posterior odds appear to confer with the idea of novelty detection; those lesions that demonstrate significant change after treatment tend to move far beyond the credible region, whilst those with low posterior odds ( $< 1/3$ ) remain within the credible region.

In these examples it is clear that inter-patient and intra-patient/inter-lesion response heterogeneity is evident within these cohorts. For those lesions that do change significantly we highlight that there is also divergence in the direction of change; whilst the vast majority of changing lesions tend to demonstrate an increase in the proportion of voxels with

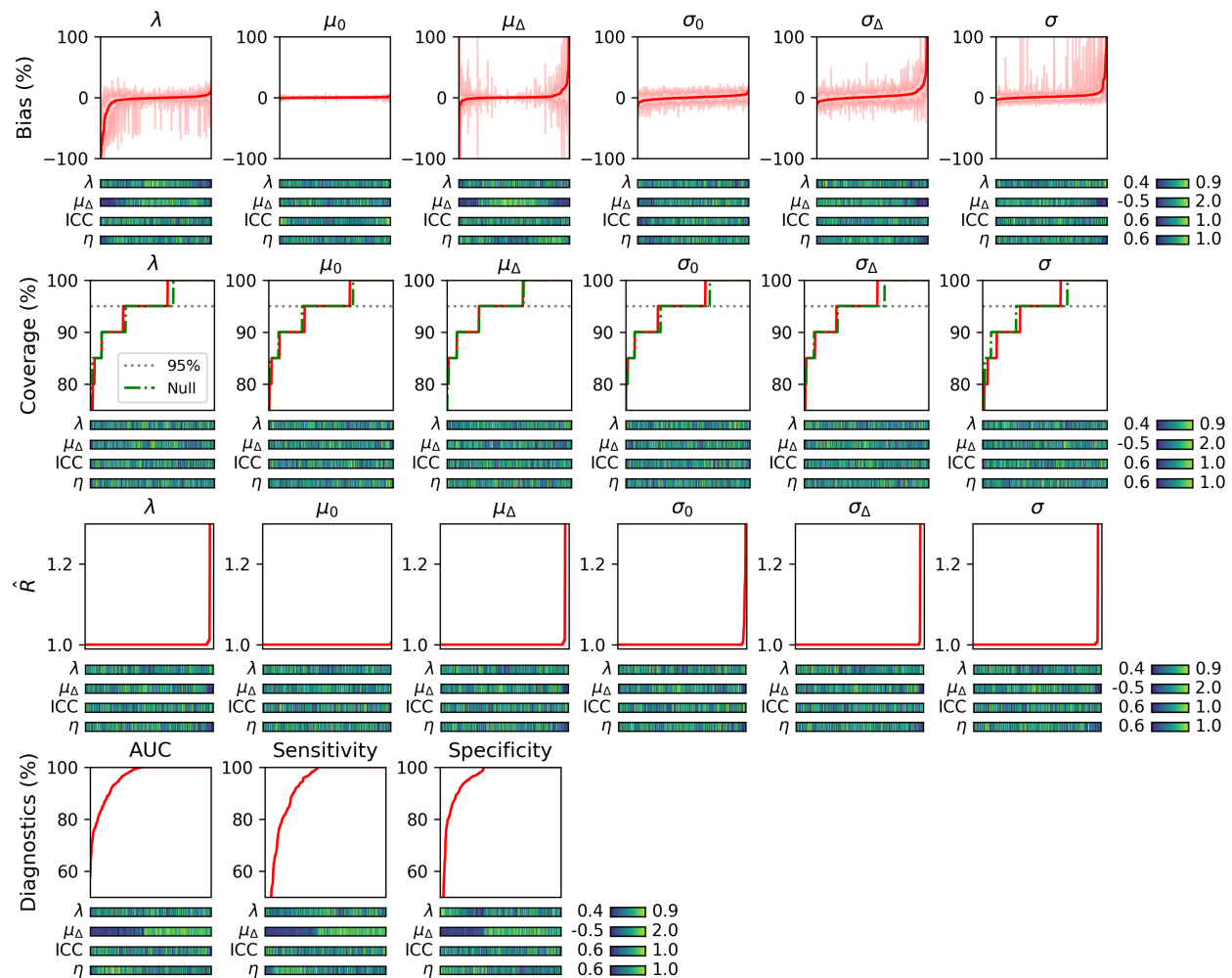


Figure 5: Simulation results for real-valued biomarkers (median ADC in this instance). The **top row** displays the percentage bias in all estimated model parameters. The solid red line represents the median estimates across 20 data repetitions for each combination of true parameters, while the pink region indicates the 10th to 90th percentile range. Values are ordered from smallest to largest bias, with potential explanatory parameters shown in the color bar below (also ordered by median bias). No significant bias is observed for any combination of explanatory parameters; however, low  $\mu_{\Delta}$  has the most notable influence. The **second row** demonstrates the coverage of the derived posterior distributions, defined as the proportion of cases where the true parameter falls within the 95% high-density interval (HDI) of the posterior. For context, a null coverage curve is included, derived by randomly sampling a standard normal variate and calculating the frequency with which it falls within the empirical 95% confidence interval, then ordering the results. The close agreement between the empirical and null coverage curves confirms that the estimator achieves the expected nominal coverage. The **third row** illustrates the median Rubin-Gelman statistic ( $\hat{R}$ ) across all simulations for each parameter combination. Excellent convergence ( $\hat{R} \rightarrow 1$ ) is observed for most parameter combinations, except in a small region where  $\mu_{\Delta} \rightarrow 0$  and  $\eta \rightarrow 0.5$ . In this region, model assumptions are violated due to minimal differences between baseline and post-treatment data. The **bottom row** depicts diagnostic metrics of log- $PO_{10}$  for the simulation studies. Performance improves with increasing  $\mu_{\Delta}$  and/or  $\eta$ , as larger expected differences between changing and non-changing biomarkers enhance model accuracy.

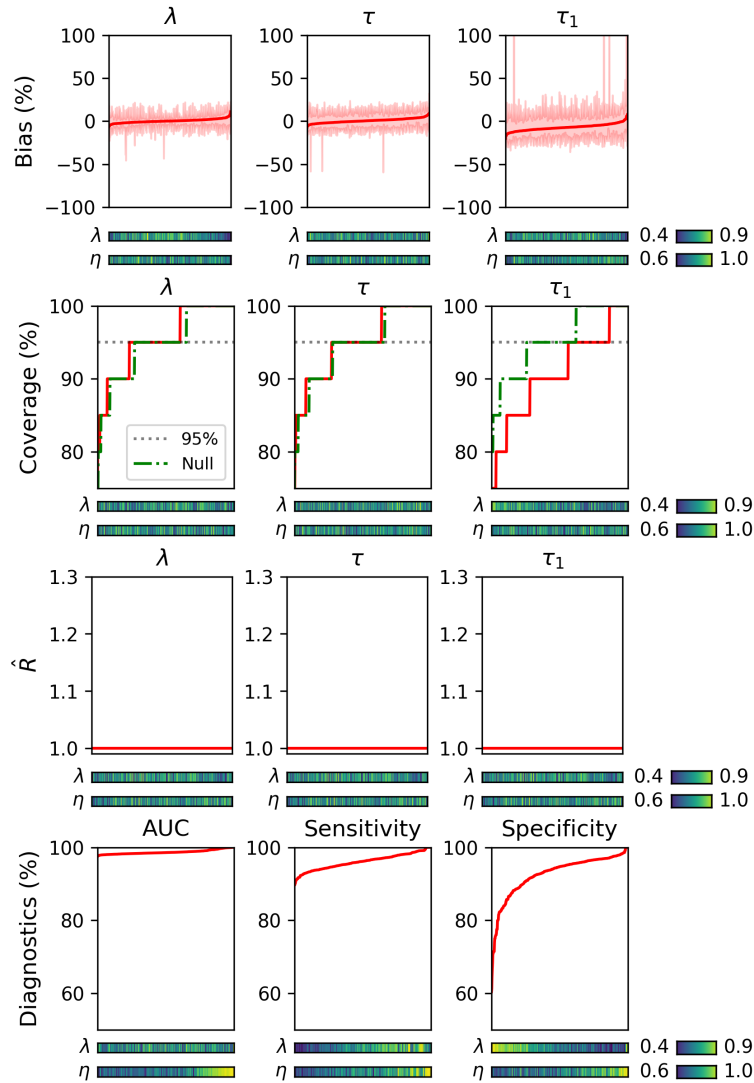


Figure 6: Simulation results for dirichlet-multinomial (habitat) biomarkers (median ADC in this instance). All results are displayed in the same format as for real variables (Figure 5). Again, we observe no significant evidence of substantial bias in estimators (top row), and observe good convergence for all parameters of interest (third row). Good coverage is observed for parameters  $\tau$  and  $\lambda$ , but mildly poorer coverage than the null curve for  $\tau_1$  (second row). Finally, there is an improvement in diagnostic performance (bottom row) as  $\eta$  increases, whilst an increase in  $\lambda$  leads to improved sensitivity but poorer specificity.

higher ADC than baseline (figure 7e for example), there are some that show a general decrease in ADC (figure 7d), and also a patient that demonstrates clear intra-tumour heterogeneity in ADC changes (figure 7a).

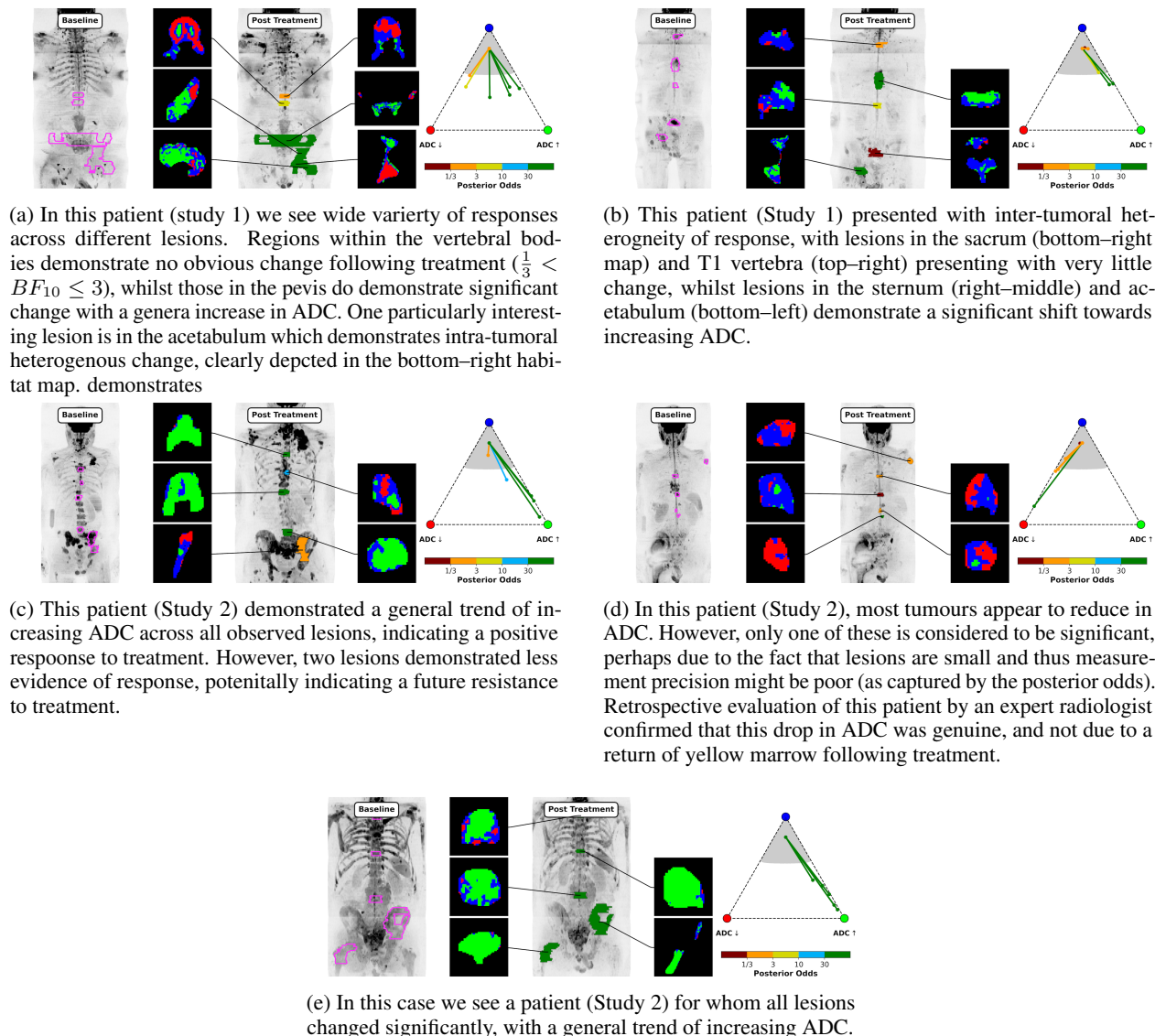


Figure 7: Example results for five patient evaluated in this study. We have presented a Maximum Intensity Projection (MIP) with lesions colour-coded according to the derived posterior odds. Habitat maps (central slice) are displayed as an overlay on the ADC map for each lesion, and a summary of inter-lesion changes can be observed in the triangular plots depicting the normalised habitat simplexes in barycentric coordinates. All imaging data are presented with identical windowing settings.

These observations are further verified in figure 8 which demonstrates the changes occurring in all lesions across both studies. Whilst the majority of lesions demonstrate a significant increase in the proportion of voxels with high ADC value, there are many that do not demonstrate any change (maroon colored lines) and several that significantly change in the other direction (signalling an increase in the number of voxels with lower ADC). Moreover, in Figure 9, we present the posterior distributions for mixing weights ( $\lambda$ ) for each study. In both cases, there is evidence that  $\lambda$  is significantly below 1, illustrating presence of response heterogeneity amongst individual lesions. This is true for both median ADC and habitat biomarkers.

To compare the posterior odds derived from both median ADC and habitat biomarkers, a scatter plot of  $\log-PO_{10}$  for both markers is presented in figure 10. There is a significant positive correlation between both, indicating that they

may convey similar information. However, this association is not perfect, indicating that they may indeed demonstrate different information in certain lesions.

### 4.3 Prior Sensitivity Analysis

To evaluate the sensitivity of our model fit to the choice of prior, we conducted a prior sensitivity analysis, with results presented in Figure 11 for Study 1 and Supplementary Figure 12 for Study 2. In this analysis, we varied the prior widths for the ADC median model ( $\sigma_\mu$  and  $\gamma_\sigma$ , Table 1) and for the habitat model ( $\gamma_\tau$ , Table 3). The posterior distributions of the following parameters were estimated both with and without the inclusion of post-treatment data:  $\sigma$ ,  $\sigma_0$ , and  $\mu_0$  for median ADC biomarkers, and  $\tau$  for habitat biomarkers.

As expected, we observed that narrow priors ( $\sigma_\mu \leq 0.1 \times 10^{-3} \text{ mm}^2/\text{s}$ ) influence the inference of the estimated distributions. However, less informative priors had a smaller impact on the posterior estimates, indicating greater robustness of the model to these choices. In general, the inclusion of post-treatment data had minimal effect on the posterior distributions. An exception to this trend was observed in the estimation of measurement precision ( $\tau$ ) for habitat biomarkers in Study 1. This discrepancy may suggest some misalignment between the assumed model and the acquired post-treatment data. In such cases, we recommend relying on estimates derived solely from repeat baseline data, as we have done when calculating credible intervals for novelty detection.

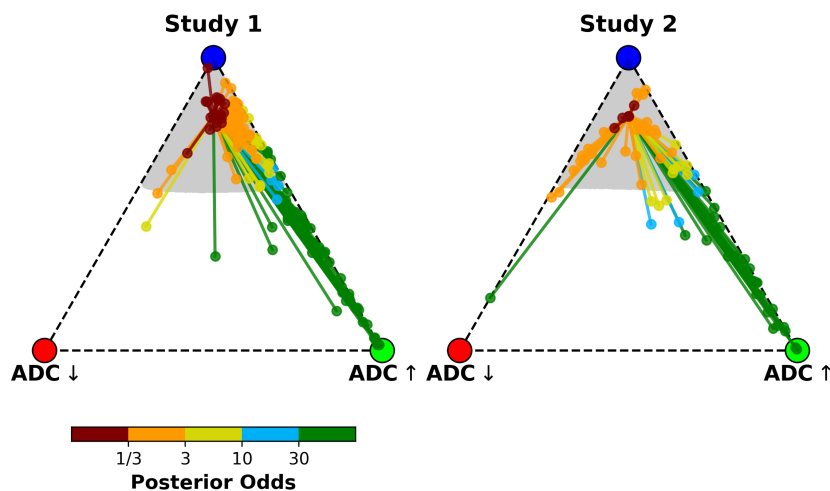


Figure 8: Barycentric coordinate plots of all lesions within both studies. For each lesion, its derived posterior odds is depicted as a color-coding, and the credible regions for identifying ‘anomalies’ is shown as a grey shaded area.

## 5 Discussion

In this article, we aim to develop a novel framework for detecting heterogeneous tumour responses in clinical studies. The application of Bayesian theory to assessing biomarker precision in cancer imaging is somewhat underutilized, particularly given recent advancements in Markov-Chain Monte-Carlo (MCMC) algorithms, including Hamiltonian Monte Carlo (HMC), and their efficient and generalized implementations for posterior parameter sampling. We propose that the detection of cancer treatment response can be framed as a decision between two competing models in a biomarker study: one where the underlying true biomarker has changed (the alternative model) and one where it has not (the null model). The goal of Bayesian analysis then is to quantify this choice by considering the precision of the measurement device and any other parameters that describe the population distribution of the biomarkers. We explore two Bayesian approaches to quantify the choice between these models: anomaly detection and Bayes factors (or their close equivalent the Posterior Odds ( $PO_{10}$ )).

Through theoretical analysis, we have demonstrated that anomaly detection closely parallels conventional practices in response biomarker assessment. In both approaches, the primary objective is to test and potentially reject the null hypothesis of no change in a biomarker for a patient, based on measurements taken before and after an intervention (e.g., treatment). This assessment is conducted at a predefined significance level, leveraging dedicated test-retest baseline biomarker data (ideally in a similar population) to derive the parameters of the null model (including measurement

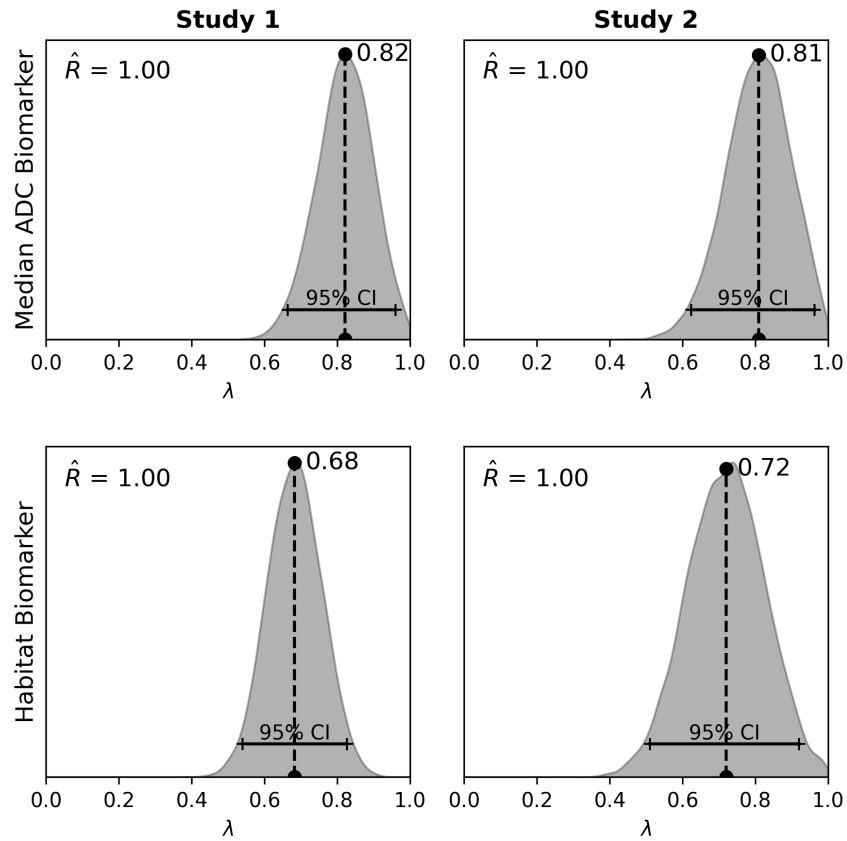


Figure 9: Kernel density plots of the posterior distributions for the mixing weight  $\lambda$ , shown alongside the median estimate (vertical dashed line), and the Rubin-Gelman statistic ( $\hat{R}$ ).

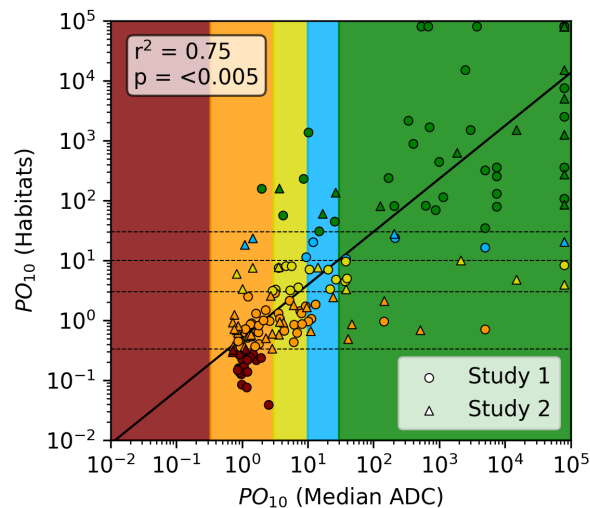


Figure 10: A comparison of  $\log-PO_{10}$  derived for median ADC within each lesion and for habitats defined for each region. Note that our estimation method for  $PO_{10}$  can lead to infinite values. These were capped to 80,000 and not included in estimation of  $r^2$  or the p-value. Vertical colors represent the  $PO_{10}$  classifications defined in section 4.2 for the median ADC data, whilst the symbol colors represent the  $PO_{10}$  for the habitat data. Data from studies 1 and 2 are separated by symbol shape.

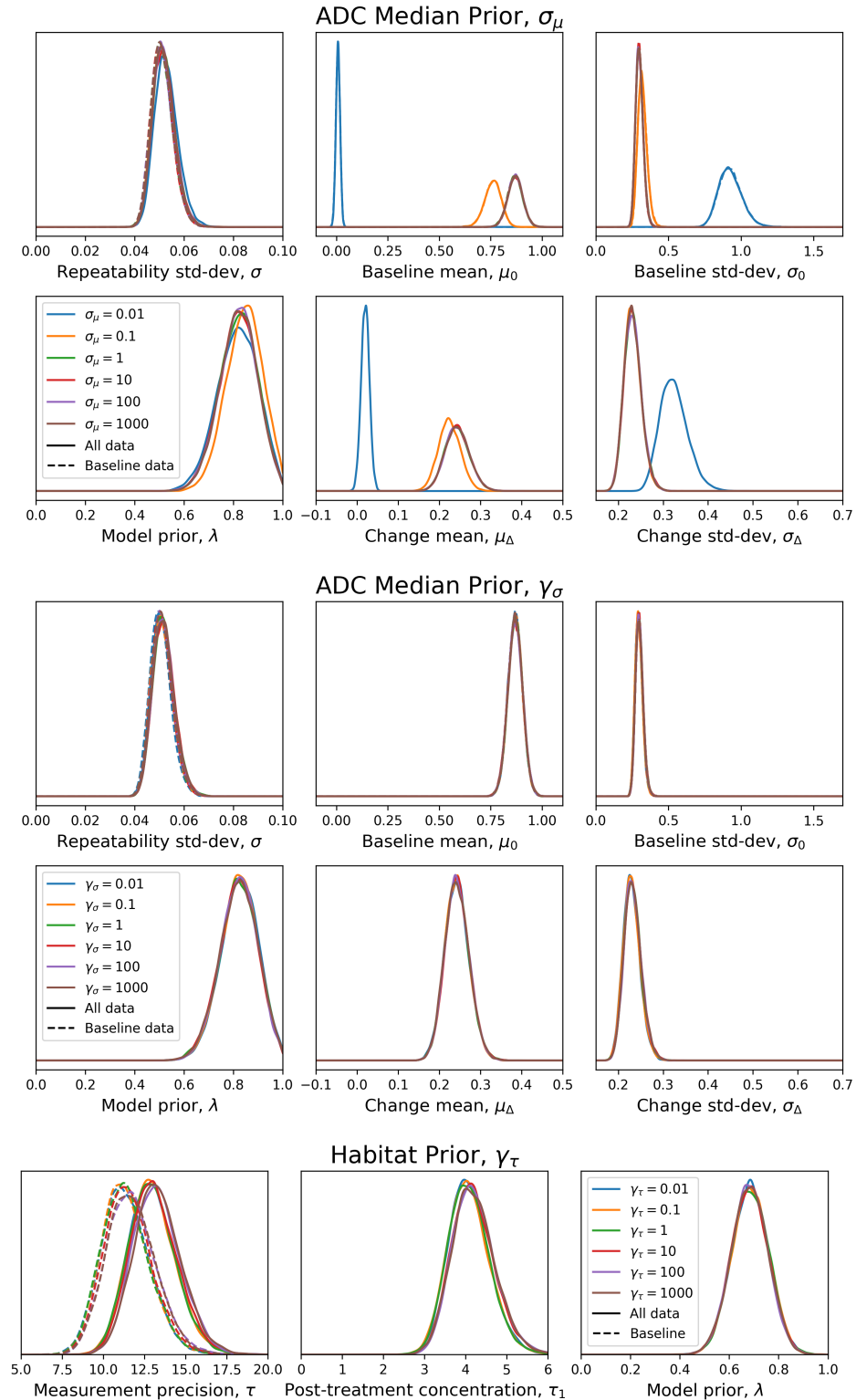


Figure 11: Prior sensitivity analysis for Study 1. The primary prior parameter influencing the posterior distributions was  $\sigma_\mu$ , which defines the width of the zero-mean normal prior for  $\mu_0$  and  $\mu_\Delta$  in ADC median biomarkers. For habitat biomarkers (bottom row), the inclusion of post-treatment data in the model fit (solid curves) notably affected the estimation of measurement precision ( $\tau$ ). For ADC median biomarkers, all parameters except  $\lambda$  are expressed in units of  $\times 10^{-3} \text{ mm}^2/\text{s}$ .

precision) and the observed post-treatment change for the patient. Integrating this method into a Bayesian framework, however, exposes the underlying assumptions of the model that can be overlooked and may not be valid in practice. For instance, we illustrate that conventional Bland-Altman analysis often assumes an infinite possible range for the biomarker, which may not be realistic—particularly in the case of quantitative imaging biomarkers, where measurements are typically bounded by physical or biological constraints. Bayesian analysis, facilitated by numerical MCMC sampling, allows us to relax these assumptions. It provides a comprehensive characterization of the uncertainties inherent in all estimated model parameters and, perhaps most importantly, it enables the assessment of biomarkers that are not univariate variables, a topic we explore extensively in this article.

We have also explored theoretical interpretations of Bayes factors in response biomarker studies. Notably, we demonstrated that Bayes factors can incorporate expected post-treatment changes into the decision-making process by integrating parameters from the alternative model. A key advantage of using Bayes factors is their ability to help researchers evaluate whether the data provide sufficient evidence to support the null model, allowing for the conclusion that there has been no change following the intervention. However, caution is warranted. Unlike the null model, estimating parameters for the alternative model can be challenging due to the difficulty of obtaining controlled experimental data. Identifying lesions or subjects that have responded to an intervention is often complex and may, in fact, be the primary role of the imaging biomarker itself. To address this, we propose that Bayesian mixture modeling offers a robust solution. This approach simultaneously estimates the parameters of the alternative model and quantifies posterior odds (equivalent to Bayes factors when the prior probability for each data model is the same) for each subject in the study.

To illustrate the efficacy of these methods, we applied them in studies evaluating the response to two systemic treatments for metastatic castrate-resistant prostate cancer (mCRPC) using whole-body diffusion-weighted MRI (WBDWI). These studies demonstrated that posterior odds estimates detect significant changes in individual lesions. Furthermore, color-coding lesions according to their posterior odds offers a practical visualization method, highlighting the heterogeneity of response both among patients and between lesions within a single patient. Use of Bayesian mixture modeling enabled the quantification of this response heterogeneity, revealing a consistent response rate of approximately 70% across both studies. Our framework incorporated habitat mapping from ADC maps directly into the decision-making process, providing detailed visualizations of changing regions within the lesions.

It is crucial to emphasize that Bayesian techniques rely on the careful definition of the underlying models. These models should be developed collaboratively with domain experts and those with expertise in probabilistic modeling to ensure their validity and applicability. Dedicated simulation studies, such as those conducted in this work, are invaluable for demonstrating that effective parameter inference is achievable for well-defined models. In addition, prior sensitivity analysis is a critical component of any Bayesian study. This step ensures that the chosen prior distribution—unless specifically and carefully selected—does not unduly influence or bias the final results, as highlighted by Depaoli et al. [2020]. Moreover, it is crucial that the test-retest data used to determine parameters in the response model are representative of the data to which the model will be applied. The size of the test-retest cohorts plays a significant role in influencing the accuracy of biomarker precision estimates, which, in turn, directly impacts the reliability and validity of model comparisons.

A slight limitation of this study is that we have treated spatially isolated lesions as independent. This approach was necessary due to the relatively small number of lesions delineated per patient in our dataset. One of the significant advantages of Bayesian methods in biomarker studies is their natural ability to incorporate inter- and intra-patient correlations in biomarker changes through hierarchical modelling Donners et al. [2024]. Looking ahead, for cases where a large number of lesions are delineated within a single patient, it would be feasible to model a per-patient response heterogeneity index,  $\lambda_i$  for  $i \in 1, \dots, N$  patients. This could include a complete characterization of the posterior distribution for these parameters, offering a more comprehensive understanding of intra-patient response variability. Applying these techniques in the clinic will eventually require automatic delineation of multiple Regions of Interest (ROIs) across various time points in whole-body imaging. This task, necessitating an experienced radiologist, can be labor-intensive. There are promising areas of research, such as the use of artificial intelligence (AI) to automate this process, potentially reducing costs and facilitating clinical adoption Candito et al. [2024], Ceranka et al. [2020].

From a technical perspective, we acknowledge potential improvements in our approach to calculating Bayes factors. Techniques like bridge sampling Gronau et al. [2017] have shown greater stability in computing Bayes factors compared to other methods. However, current implementations primarily support complete model comparisons and do not extend to estimating individual subjects within a study via mixture models, as we have explored. Future work could investigate adapting bridge sampling for this purpose. Moreover, our study does not include biological validation of the techniques, as our primary aim was to establish a theoretical framework for assessing the repeatability of tumor response heterogeneity measurements. Future research might validate these methods through targeted biopsy or surgical specimen analysis Donners et al. [2022], linking our results with promising directions in digital histopathology Zhu

et al. [2023] and spatial gene expression profiling Brady et al. [2021]. Ultimately, assessing the clinical utility of our approach will require larger patient studies with access to relevant clinical end-points such as progression-free survival or overall survival Perez-Lopez et al. [2017, 2016].

It is important to recognize the breadth of machine learning tools available for novelty detection that could be explored for tumor response analysis. These tools range from isolation forests Liu et al. [2008] and one-class support vector machines Schölkopf et al. [2001] to deep learning approaches like autoencoders Pidhorskyi et al. [2018] and Siamese networks Liu et al. [2022]. A significant advantage of these methods is their ability to operate without predefined data models. However, they generally require access to large datasets, which may not always be available, particularly for less common cancer types or specific imaging modalities. Additionally, unlike Bayesian methods, these approaches generally do not inherently account for uncertainty in their decision-making processes, an essential feature for any clinical decision-support tool. An additional research area of interest here is the application of more informative prior distributions to model parameters. While we have opted for uninformative priors to avoid biasing our results, Bayesian techniques inherently facilitate adaptive learning. More informative priors could effectively integrate data from previous similar studies into the decision-making process, enhancing the accuracy and relevance of the models. Finally, we note that although have focussed on the application of techniques to a single post-treatment scans, these methods can be adapted to biomarker studies with multiple post-treatment imaging studies for longitudinal assessment. However, this will depend on the ability to integrate these methods into a medical device that helps clinicians understand and visualize the complex changes occurring over time.

Bayesian methods in response biomarker studies present significant advantages over traditional statistical approaches. One of their most crucial benefits is the ability to analyze imaging features beyond normally-distributed biomarkers, a topic we have extensively explored in this article. This is particularly evident in habitat imaging which is emerging as a valuable technique for performing “virtual biopsies”, and links the intra-tumoral heterogeneity captured from radiological imaging to the underlying pathological and biological mechanisms. Accurate characterization of habitats can be used to guide radiotherapy treatment to target the most aggressive tumour areas, guide surgical biopsies and monitor treatment response Paverd et al. [2024]. We anticipate that frameworks such as ours are essential to assess the validity of such approaches and support their integration in the clinical setting by providing clinicians with a clear and interpretable summary of which tumors in each patient are showing significant changes post-treatment. This could offer an early opportunity to modify or intensify treatments in areas showing resistance, potentially improving patient outcomes and further advancing personalized medicine.

## 6 Acknowledgements

This study represents independent research supported by the National Institute for Health and Care Research (NIHR) Biomedical Research Centre and the Clinical Research Facility in Imaging at The Royal Marsden NHS Foundation Trust and the Institute of Cancer Research, London. The views expressed are those of the author(s) and not necessarily those of the NIHR or the Department of Health and Social Care.

## 7 Declaration of generative AI and AI-assisted technologies in the writing process

During the preparation of this work the authors used ChatGPT to improve grammar within the paper only. After using this service, the authors reviewed and edited the content as needed and take full responsibility for the content of the publication.

## References

- Robert J Gillies, Paul E Kinahan, and Hedvig Hricak. Radiomics: Images are more than pictures, they are data. *Radiology*, 278(2):563–77, Feb 2016. doi:10.1148/radiol.2015151169.
- James P B O’Connor, Eric O Aboagye, Judith E Adams, Hugo J W L Aerts, Sally F Barrington, Ambros J Beer, Ronald Boellaard, Sarah E Bohndiek, Michael Brady, Gina Brown, David L Buckley, Thomas L Chenevert, Laurence P Clarke, Sandra Collette, Gary J Cook, Nandita M deSouza, John C Dickson, Caroline Dive, Jeffrey L Evelhoch, Corinne Faivre-Finn, Ferdia A Gallagher, Fiona J Gilbert, Robert J Gillies, Vicky Goh, John R Griffiths, Ashley M Groves, Steve Halligan, Adrian L Harris, David J Hawkes, Otto S Hoekstra, Erich P Huang, Brian F Hutton, Edward F Jackson, Gordon C Jayson, Andrew Jones, Dow-Mu Koh, Denis Lacombe, Philippe Lambin, Nathalie Lassau, Martin O Leach, Ting-Yim Lee, Edward L Leen, Jason S Lewis, Yan Liu, Mark F Lythgoe, Prakash Manoharan, Ross J Maxwell, Kenneth A Miles, Bruno Morgan, Steve Morris, Tony Ng, Anwar R Padhani, Geoff J M Parker, Mike Partridge, Arvind P Pathak, Andrew C Peet, Shonit Punwani, Andrew R Reynolds, Simon P Robinson,

- Lalitha K Shankar, Ricky A Sharma, Dmitry Soloviev, Sigrid Stroobants, Daniel C Sullivan, Stuart A Taylor, Paul S Tofts, Gillian M Tozer, Marcel van Herk, Simon Walker-Samuel, James Wason, Kaye J Williams, Paul Workman, Thomas E Yankeelov, Kevin M Brindle, Lisa M McShane, Alan Jackson, and John C Waterton. Imaging biomarker roadmap for cancer studies. *Nat Rev Clin Oncol*, 14(3):169–186, Mar 2017. doi:10.1038/nrclinonc.2016.162.
- E. A. Eisenhauer, P. Therasse, J. Bogaerts, L. H. Schwartz, D. Sargent, R. Ford, J. Dancey, S. Arbuck, S. Gwyther, M. Mooney, L. Rubinstein, L. Shankar, L. Dodd, R. Kaplan, D. Lacombe, and J. Verweij. New response evaluation criteria in solid tumours: revised recist guideline (version 1.1). *European journal of cancer (Oxford, England : 1990)*, 45:228–247, 1 2009. ISSN 1879-0852. doi:10.1016/J.EJCA.2008.10.026. URL <https://pubmed.ncbi.nlm.nih.gov/19097774/>.
- Elizabeth M Charles-Edwards and Nandita M deSouza. Diffusion-weighted magnetic resonance imaging and its application to cancer. *Cancer Imaging*, 6(1):135–43, Sep 2006. doi:10.1102/1470-7330.2006.0021.
- Dow-Mu Koh and David J Collins. Diffusion-weighted mri in the body: applications and challenges in oncology. *AJR Am J Roentgenol*, 188(6):1622–35, Jun 2007. doi:10.2214/AJR.06.1403.
- Alexey Surov, Hans Jonas Meyer, and Andreas Wienke. Correlation between apparent diffusion coefficient (adc) and cellularity is different in several tumors: a meta-analysis. *Oncotarget*, 8(35):59492–59499, Aug 2017. doi:10.18632/oncotarget.17752.
- Armando Manduca, Philip J Bayly, Richard L Ehman, Arunark Kolipaka, Thomas J Royston, Ingolf Sack, Ralph Sinkus, and Bernard E Van Beers. Mr elastography: Principles, guidelines, and terminology. *Magn Reson Med*, 85(5):2377–2390, May 2021. doi:10.1002/mrm.28627.
- Ingolf Sack. Magnetic resonance elastography from fundamental soft-tissue mechanics to diagnostic imaging. *Nature Reviews Physics*, 5(1):25–42, 2023. doi:10.1038/s42254-022-00543-2. URL <https://doi.org/10.1038/s42254-022-00543-2>.
- M O Leach, B Morgan, P S Tofts, D L Buckley, W Huang, M A Horsfield, T L Chenevert, D J Collins, A Jackson, D Lomas, B Whitcher, L Clarke, R Plummer, I Judson, R Jones, R Alonzi, T Brunner, D M Koh, P Murphy, J C Waterton, G Parker, M J Graves, T W J Scheenen, T W Redpath, M Orton, G Karczmar, H Huisman, J Barentsz, A Padhani, and Experimental Cancer Medicine Centres Imaging Network Steering Committee. Imaging vascular function for early stage clinical trials using dynamic contrast-enhanced magnetic resonance imaging. *Eur Radiol*, 22(7):1451–64, Jul 2012. doi:10.1007/s00330-012-2446-x.
- Parvinder Sujlana, Jan Skrok, and Laura M Fayad. Review of dynamic contrast-enhanced mri: Technical aspects and applications in the musculoskeletal system. *J Magn Reson Imaging*, 47(4):875–890, Apr 2018. ISSN 1522-2586 (Electronic); 1053-1807 (Linking). doi:10.1002/jmri.25810.
- Emily Hoffmann, Max Masthoff, Wolfgang G Kunz, Max Seidensticker, Stefanie Bobe, Mirjam Gerwing, Wolfgang E Berdel, Christoph Schliemann, Cornelius Faber, and Moritz Wildgruber. Multiparametric mri for characterization of the tumour microenvironment. *Nat Rev Clin Oncol*, Apr 2024. doi:10.1038/s41571-024-00891-1.
- Nicholas McGranahan and Charles Swanton. Biological and therapeutic impact of intratumor heterogeneity in cancer evolution. *Cancer Cell*, 27(1):15–26, Jan 2015. doi:10.1016/j.ccell.2014.12.001.
- Carlo C Maley, Athena Aktipis, Trevor A Graham, Andrea Sottoriva, Amy M Boddy, Michalina Janiszewska, Ariosto S Silva, Marco Gerlinger, Yinyin Yuan, Kenneth J Pienta, Karen S Anderson, Robert Gatenby, Charles Swanton, David Posada, Chung-I Wu, Joshua D Schiffman, E Shelley Hwang, Kornelia Polyak, Alexander R A Anderson, Joel S Brown, Mel Greaves, and Darryl Shibata. Classifying the evolutionary and ecological features of neoplasms. *Nat Rev Cancer*, 17(10):605–619, Oct 2017. doi:10.1038/nrc.2017.69.
- Sarah R Amend and Kenneth J Pienta. Ecology meets cancer biology: the cancer swamp promotes the lethal cancer phenotype. *Oncotarget*, 6(12):9669–78, 2015. doi:10.18632/oncotarget.3430.
- E Sala, E Mema, Y Himoto, H Veeraraghavan, J D Brenton, A Snyder, B Weigelt, and H A Vargas. Unravelling tumour heterogeneity using next-generation imaging: radiomics, radiogenomics, and habitat imaging. *Clin Radiol*, 72(1): 3–10, Jan 2017. doi:10.1016/j.crad.2016.09.013.
- Mireia Crispin-Ortuzar, Marcel Gehrung, Stephan Ursprung, Andrew B Gill, Anne Y Warren, Lucian Beer, Ferdia A Gallagher, Thomas J Mitchell, Iosif A Mendichovszky, Andrew N Priest, Grant D Stewart, Evis Sala, and Florian Markowetz. Three-dimensional printed molds for image-guided surgical biopsies: An open source computational platform. *JCO Clin Cancer Inform*, 4:736–748, Aug 2020. doi:10.1200/CCI.20.00026.
- Lucian Beer, Paula Martin-Gonzalez, Maria Delgado-Ortet, Marika Reinius, Leonardo Rundo, Ramona Woitek, Stephan Ursprung, Lorena Escudero, Hilal Sahin, Ionut-Gabriel Funingana, Joo-Ern Ang, Mercedes Jimenez-Linan, Tristan Lawton, Gaurav Phadke, Sally Davey, Nghia Q Nguyen, Florian Markowetz, James D Brenton, Mireia Crispin-Ortuzar, Helen Addley, and Evis Sala. Ultrasound-guided targeted biopsies of ct-based radiomic tumour habitats:

- technical development and initial experience in metastatic ovarian cancer. *Eur Radiol*, 31(6):3765–3772, Jun 2021. doi:10.1007/s00330-020-07560-8.
- Konstantinos Zormpas-Petridis, Evon Poon, Matthew Clarke, Neil P Jerome, Jessica K R Boulton, Matthew D Blackledge, Fernando Carceller, Alexander Koers, Giuseppe Barone, Andrew D J Pearson, Lucas Moreno, John Anderson, Neil Sebire, Kieran McHugh, Dow-Mu Koh, Louis Chesler, Yinyin Yuan, Simon P Robinson, and Yann Jamin. Noninvasive mri native t1 mapping detects response to mycn-targeted therapies in the th-mycn model of neuroblastoma. *Cancer Res*, 80(16):3424–3435, Aug 2020. doi:10.1158/0008-5472.CAN-20-0133.
- Camilla Panico, Giacomo Avesani, Konstantinos Zormpas-Petridis, Leonardo Rundo, Camilla Nero, and Evis Sala. Radiomics and radiogenomics of ovarian cancer: Implications for treatment monitoring and clinical management. *Radiol Clin North Am*, 61(4):749–760, Jul 2023. doi:10.1016/j.rcl.2023.02.006.
- Nancy A Obuchowski. Interpreting change in quantitative imaging biomarkers. *Acad Radiol*, 25(3):372–379, Mar 2018. ISSN 1878-4046 (Electronic); 1076-6332 (Print); 1076-6332 (Linking). doi:10.1016/j.acra.2017.09.023.
- Nancy A. Obuchowski and Andrew J. Buckler. Estimating the precision of quantitative imaging biomarkers without test-retest studies. *Academic Radiology*, 29(4):543–549, 2022. ISSN 1076-6332. doi:https://doi.org/10.1016/j.acra.2021.06.009. URL https://www.sciencedirect.com/science/article/pii/S1076633221002798.
- Jessica M Winfield, Nina Tunariu, Mihaela Rata, Keiko Miyazaki, Neil P Jerome, Michael Germuska, Matthew D Blackledge, David J Collins, Johann S de Bono, Timothy A Yap, Nandita M deSouza, Simon J Doran, Dow-Mu Koh, Martin O Leach, Christina Messiou, and Matthew R Orton. Extracranial soft-tissue tumors: Repeatability of apparent diffusion coefficient estimates from diffusion-weighted mr imaging. *Radiology*, 284(1):88–99, Jul 2017. doi:10.1148/radiol.2017161965.
- Jessica M Winfield, Aisha B Miah, Dirk Strauss, Khin Thway, David J Collins, Nandita M deSouza, Martin O Leach, Veronica A Morgan, Sharon L Giles, Eleanor Moskovic, Andrew Hayes, Myles Smith, Shane H Zaidi, Daniel Henderson, and Christina Messiou. Utility of multi-parametric quantitative magnetic resonance imaging for characterization and radiotherapy response assessment in soft-tissue sarcomas and correlation with histopathology. *Front Oncol*, 9:280, 2019. doi:10.3389/fonc.2019.00280.
- J. Martin Bland and Douglas G. Altman. Statistical methods for assessing agreement between two methods of clinical measurement. *The Lancet*, 327:307–310, 2 1986. ISSN 0140-6736. doi:10.1016/S0140-6736(86)90837-8.
- Howard I. Scher, Michael J. Morris, Walter M. Stadler, Celestia Higano, Ethan Basch, Karim Fizazi, Emmanuel S. Antonarakis, Tomasz M. Beer, Michael A. Carducci, Kim N. Chi, Paul G. Corn, Johann S. De Bono, Robert Dreicer, Daniel J. George, Elisabeth I. Heath, Maha Hussain, Wm Kevin Kelly, Glenn Liu, Christopher Logothetis, David Nanus, Mark N. Stein, Dana E. Rathkopf, Susan F. Slovin, Charles J. Ryan, Oliver Sartor, Eric J. Small, Matthew Raymond Smith, Cora N. Sternberg, Mary Ellen Taplin, George Wilding, Peter S. Nelson, Lawrence H. Schwartz, Susan Halabi, Philip W. Kantoff, and Andrew J. Armstrong. Trial design and objectives for castration-resistant prostate cancer: Updated recommendations from the prostate cancer clinical trials working group 3. *Journal of Clinical Oncology*, 34, 2016. ISSN 15277755. doi:10.1200/JCO.2015.64.2702.
- Matthew D. Blackledge, David J. Collins, Nina Tunariu, Matthew R. Orton, Anwar R. Padhani, Martin O. Leach, and Dow Mu Koh. Assessment of treatment response by total tumor volume and global apparent diffusion coefficient using diffusion-weighted mri in patients with metastatic bone disease: A feasibility study. *PLoS ONE*, 9, 2014. ISSN 19326203. doi:10.1371/journal.pone.0091779.
- Anwar R. Padhani, Frederic E. Lecouvet, Nina Tunariu, Dow Mu Koh, Frederik De Keyzer, David J. Collins, Evis Sala, Heinz Peter Schlemmer, Giuseppe Petralia, H. Alberto Vargas, Stefano Fanti, H. Bertrand Tombal, and Johann de Bono. Metastasis reporting and data system for prostate cancer: Practical guidelines for acquisition, interpretation, and reporting of whole-body magnetic resonance imaging-based evaluations of multiorgan involvement in advanced prostate cancer [figure presente]. *European Urology*, 71:81–92, 2017. ISSN 18737560. doi:10.1016/j.eururo.2016.05.033.
- Anne M. Euser, Friedo W. Dekker, and Saskia le Cessie. A practical approach to bland-altman plots and variation coefficients for log transformed variables. *Journal of Clinical Epidemiology*, 61(10):978–982, 2008. ISSN 0895-4356. doi:https://doi.org/10.1016/j.jclinepi.2007.11.003. URL https://www.sciencedirect.com/science/article/pii/S0895435607004131.
- Nancy A Obuchowski, Erich Huang, Nandita M deSouza, David Raunig, Jana Delfino, Andrew Buckler, Charles Hatt, Xiaofeng Wang, Chaya Moskowitz, Alexander Guimaraes, Maryellen Giger, Timothy J Hall, Paul Kinahan, and Gene Pennello. A framework for evaluating the technical performance of multiparameter quantitative imaging biomarkers (mp-qibs). *Acad Radiol*, 30(2):147–158, Feb 2023. doi:10.1016/j.acra.2022.08.031.

- Andrew Gelman and Donald B Rubin. Inference from iterative simulation using multiple sequences. *Statistical science*, 7(4):457–472, 1992.
- Quentin F Gronau, Alexandra Sarafoglou, Dora Matzke, Alexander Ly, Udo Boehm, Maarten Marsman, David S Leslie, Jonathan J Forster, Eric-Jan Wagenmakers, and Helen Steingroever. A tutorial on bridge sampling. *J Math Psychol*, 81:80–97, Dec 2017. doi:10.1016/j.jmp.2017.09.005.
- Michael D Lee and Eric-Jan Wagenmakers. *Bayesian cognitive modeling: A practical course*. Cambridge university press, 2014.
- Imogen Thrussell, Jessica M Winfield, Matthew R Orton, Aisha B Miah, Shane H Zaidi, Amani Arthur, Khin Thway, Dirk C Strauss, David J Collins, Dow-Mu Koh, Uwe Oelfke, Paul H Huang, James P B O’Connor, Christina Messiou, and Matthew D Blackledge. Radiomic features from diffusion-weighted mri of retroperitoneal soft-tissue sarcomas are repeatable and exhibit change after radiotherapy. *Front Oncol*, 12:899180, 2022. doi:10.3389/fonc.2022.899180.
- Dow-Mu Koh, Matthew Blackledge, David J Collins, Anwar R Padhani, Toni Wallace, Benjamin Wilton, N Jane Taylor, J James Stirling, Rajesh Sinha, Pat Walicke, Martin O Leach, Ian Judson, and Paul Nathan. Reproducibility and changes in the apparent diffusion coefficients of solid tumours treated with combretastatin a4 phosphate and bevacizumab in a two-centre phase i clinical trial. *Eur Radiol*, 19(11):2728–38, Nov 2009. doi:10.1007/s00330-009-1469-4.
- Matthew David Blackledge, DM Koh, David J Collins, Erica Scurr, Julie Hughes, M Leach, et al. Assessing response heterogeneity following radium 223 administration using whole body diffusion weighted mri. In *International Society for Magnetic Resonance in Medicine 25th Annual Meeting & Exhibition*, 2017.
- Danoob Dalili, Anwar R Padhani, Robert Grimm, and Siemens Healthineers. Quantitative wb-mri with adc histogram analysis for response assessment in diffuse bone disease. *Magn. Flash*, 69:32–37, 2017.
- Ravin Kumar, Colin Carroll, Ari Hartikainen, and Osvaldo Antonio Martín. Arviz a unified library for exploratory analysis of bayesian models in python. 2019.
- Antoine Rosset, Luca Spadola, and Osman Ratib. Osirix: an open-source software for navigating in multidimensional dicom images. *J Digit Imaging*, 17(3):205–16, Sep 2004. doi:10.1007/s10278-004-1014-6.
- Matthew D Blackledge, David J Collins, Dow-Mu Koh, and Martin O Leach. Rapid development of image analysis research tools: bridging the gap between researcher and clinician with pyosirix. *Computers in biology and medicine*, 69:203–212, 2016.
- Sarah Depaoli, Sonja D Winter, and Marieke Visser. The importance of prior sensitivity analysis in bayesian statistics: demonstrations using an interactive shiny app. *Frontiers in psychology*, 11:608045, 2020.
- Ricardo Donners, Antonio Candito, Mihaela Rata, Adam Sharp, Christina Messiou, Dow-Mu Koh, Nina Tunariu, and Matthew D Blackledge. Inter-and intra-patient repeatability of radiomic features from multiparametric whole-body mri in patients with metastatic prostate cancer. *Cancers*, 16(9):1647, 2024.
- Antonio Candito, Richard Holbrey, Ana Ribeiro, Alina Dragan, Christina Messiou, Nina Tunariu, Matthew D Blackledge, and Dow-Mu Koh. Deep learning assisted atlas-based delineation of the skeleton from whole-body diffusion weighted mri in patients with malignant bone disease. *Biomedical Signal Processing and Control*, 92:106099, 2024.
- Jakub Ceranka, Frédéric Lecouvet, Johan De Mey, and Jef Vandemeulebroucke. Computer-aided detection of focal bone metastases from whole-body multi-modal mri. In *Medical Imaging 2020: Computer-Aided Diagnosis*, volume 11314, pages 174–180. SPIE, 2020.
- Ricardo Donners, Ines Figueiredo, Nina Tunariu, Matthew Blackledge, Dow-Mu Koh, Maria de Los Dolores Fenor de la Maza, Khobe Chandran, Johann S de Bono, and Nicos Fotiadis. Multiparametric bone mri can improve ct-guided bone biopsy target selection in cancer patients and increase diagnostic yield and feasibility of next-generation tumour sequencing. *Eur Radiol*, 32(7):4647–4656, Jul 2022. doi:10.1007/s00330-022-08536-6.
- Lianghui Zhu, Huijuan Shi, Huiting Wei, Chengjiang Wang, Shanshan Shi, Fenfen Zhang, Renao Yan, Yiqing Liu, Tingting He, Liyuan Wang, Junru Cheng, Hufei Duan, Hong Du, Fengjiao Meng, Wenli Zhao, Xia Gu, Linlang Guo, Yingpeng Ni, Yonghong He, Tian Guan, and Anjia Han. An accurate prediction of the origin for bone metastatic cancer using deep learning on digital pathological images. *EBioMedicine*, 87:104426, Jan 2023. doi:10.1016/j.ebiom.2022.104426.
- Lauren Brady, Michelle Kriner, Ilsa Coleman, Colm Morrissey, Martine Roudier, Lawrence D True, Roman Gulati, Stephen R Plymate, Zoey Zhou, Brian Birditt, Rhonda Meredith, Gary Geiss, Margaret Hoang, Joseph Beechem, and Peter S Nelson. Inter- and intra-tumor heterogeneity of metastatic prostate cancer determined by digital spatial gene expression profiling. *Nat Commun*, 12(1):1426, Mar 2021. doi:10.1038/s41467-021-21615-4.

- Raquel Perez-Lopez, Joaquin Mateo, Helen Mossop, Matthew D Blackledge, David J Collins, Mihaela Rata, Veronica A Morgan, Alison Macdonald, Shahneen Sandhu, David Lorente, Pasquale Rescigno, Zafeiris Zafeiriou, Diletta Bianchini, Nuria Porta, Emma Hall, Martin O Leach, Johann S de Bono, Dow-Mu Koh, and Nina Tunariu. Diffusion-weighted imaging as a treatment response biomarker for evaluating bone metastases in prostate cancer: A pilot study. *Radiology*, 283(1):168–177, Apr 2017. doi:10.1148/radiol.2016160646.
- Raquel Perez-Lopez, David Lorente, Matthew D Blackledge, David J Collins, Joaquin Mateo, Diletta Bianchini, Aurelius Omlin, Andrea Zivi, Martin O Leach, Johann S de Bono, Dow-Mu Koh, and Nina Tunariu. Volume of bone metastasis assessed with whole-body diffusion-weighted imaging is associated with overall survival in metastatic castration-resistant prostate cancer. *Radiology*, 280(1):151–60, Jul 2016. doi:10.1148/radiol.2015150799.
- Fei Tony Liu, Kai Ming Ting, and Zhi-Hua Zhou. Isolation forest. In *2008 eighth ieee international conference on data mining*, pages 413–422. IEEE, 2008.
- B Schölkopf, J C Platt, J Shawe-Taylor, A J Smola, and R C Williamson. Estimating the support of a high-dimensional distribution. *Neural Comput*, 13(7):1443–71, Jul 2001. doi:10.1162/089976601750264965.
- Stanislav Pidhorskyi, Ranya Almoheisen, and Gianfranco Doretto. Generative probabilistic novelty detection with adversarial autoencoders. *Advances in neural information processing systems*, 31, 2018.
- Xuxing Liu, Weize Gao, Rankang Li, Yu Xiong, Xiaoqin Tang, and Shanxiong Chen. One shot ancient character recognition with siamese similarity network. *Sci Rep*, 12(1):14820, Sep 2022. doi:10.1038/s41598-022-18986-z.
- Hania Paverd, Konstantinos Zormpas-Petridis, Hannah Clayton, Sarah Burge, and Mireia Crispin-Ortuzar. Radiology and multi-scale data integration for precision oncology. *NPJ Precision Oncology*, 8(1):158, 2024.
- Eric-Jan Wagenmakers, Tom Lodewyckx, Himanshu Kuriyal, and Raoul Grasman. Bayesian hypothesis testing for psychologists: a tutorial on the savage-dickey method. *Cogn Psychol*, 60(3):158–89, May 2010. doi:10.1016/j.cogpsych.2009.12.001.

## Supplementary Material

### 7.1 Mathematical derivations

**Theorem 7.1.** *If*

$$y \sim \mathcal{N}(x_0, \sigma) \quad y_0 \sim \mathcal{N}(x_0, \sigma) \quad x_0 \sim \mathcal{N}(\mu_0, \sigma_0)$$

*then*

$$p(y|y_0, \sigma, \mu_0, \sigma_0, M_0) = \mathcal{N}(\mu^*, \sigma^*) \quad (9)$$

*where*

$$\begin{aligned} \mu^* &= ICC \cdot y_0 + (1 - ICC) \cdot \mu_0 & \sigma^* &= \sqrt{1 + ICC} \cdot \sigma \\ ICC &= \frac{\sigma_0^2}{\sigma^2 + \sigma_0^2} \end{aligned}$$

*Proof.* We begin by substituting the measurement error term,  $\sigma$  for *precision*,  $\tau = \frac{1}{\sigma^2}$ , such that

$$\begin{aligned} p(y_0|x_0, \tau) &\propto \exp\left\{-\frac{\tau}{2}(y_0 - x_0)^2\right\} \\ p(y|x_0, \tau) &\propto \exp\left\{-\frac{\tau}{2}(y - x_0)^2\right\} \end{aligned}$$

Using Bayes' theorem we derive the conditional distribution of  $y$  given  $y_0$ ,  $\tau$ , and population parameters  $\mu_0$  and  $\tau_0 = \frac{1}{\sigma_0^2}$  by marginalising over the common true biomarker value  $x_0$ .

$$\begin{aligned} p(y|y_0, \tau, \mu_0, \tau_0) &\propto p(y_0, y|\tau, \mu_0, \tau_0) \\ &= \int_{-\infty}^{\infty} p(y_0, y|x_0, \tau)p(x_0|\mu_0, \tau_0)dx_0 \\ &= \int_{-\infty}^{\infty} p(y_0|x_0, \tau)p(y|x_0, \tau)p(x_0|\mu_0, \tau_0)dx_0 \end{aligned}$$

Therefore

$$\begin{aligned} &p(y|y_0, \tau, \mu_0, \tau_0) \\ &\propto \int_{-\infty}^{\infty} \exp\left\{-\frac{\tau}{2}(y_0 - x_0)^2\right\} \exp\left\{-\frac{\tau}{2}(y - x_0)^2\right\} \\ &\quad \times \exp\left\{-\frac{\tau_0}{2}(x_0 - \mu_0)^2\right\} dx_0 \\ &\propto \int_{-\infty}^{\infty} \exp\left\{-\frac{2\tau + \tau_0}{2} \left(x_0^2 - 2x_0 \frac{\tau(y_0 + y) + \tau_0\mu_0}{2\tau + \tau_0}\right)\right\} dx_0 \\ &\quad \times \exp\left\{-\frac{\tau}{2}y^2\right\} \\ &= \int_{-\infty}^{\infty} \exp\left\{-\frac{2\tau + \tau_0}{2} \left(x_0 - \frac{\tau(y_0 + y) + \tau_0\mu_0}{2\tau + \tau_0}\right)^2\right\} dx \\ &\quad \times \exp\left\{-\frac{\tau}{2}y^2\right\} \exp\left\{\frac{(\tau(y_0 + y) + \tau_0\mu_0)^2}{2(2\tau + \tau_0)}\right\} \\ &\propto \exp\left\{-\frac{\tau}{2}y^2 + \frac{\tau^2(y_0 + y)^2 + 2\tau_0\mu_0\tau y}{2(2\tau + \tau_0)}\right\} \\ &\propto \exp\left\{-\frac{\tau}{2(2\tau + \tau_0)}(y^2(\tau + \tau_0) - 2y(y_0\tau + \tau_0\mu_0))\right\} \\ &\propto \exp\left\{-\frac{1}{2} \frac{\tau(\tau + \tau_0)}{2\tau + \tau_0} \left(y - \frac{y_0\tau + \tau_0\mu_0}{\tau + \tau_0}\right)^2\right\} \end{aligned}$$

Now making the substitutions

$$\mu^* = \frac{y_0\tau + \tau_0\mu_0}{\tau + \tau_0}, \quad \tau^* = \frac{\tau(\tau + \tau_0)}{2\tau + \tau_0}$$

we deduce that

$$p(y|y_0, \tau, \mu_0, \tau_0) = \mathcal{N}\left(\mu^*, \frac{1}{\sqrt{\tau^*}}\right)$$

Lastly, we have that

$$\begin{aligned} \mu^* &= \frac{\tau}{\tau + \tau_0} \cdot y_0 + \left(1 - \frac{\tau}{\tau + \tau_0}\right) \cdot \mu_0 \\ &= \frac{\sigma_0^2}{\sigma^2 + \sigma_0^2} \cdot y_0 + \left(1 - \frac{\sigma_0^2}{\sigma^2 + \sigma_0^2}\right) \cdot \mu_0 \\ &= ICC \cdot y_0 + (1 - ICC) \cdot \mu_0 \end{aligned}$$

and

$$\begin{aligned} \sigma^* &= \sqrt{\frac{1}{\tau^*}} = \sqrt{\frac{2\tau + \tau_0}{\tau(\tau + \tau_0)}} \\ &= \sqrt{\frac{1}{\tau} \left(2 \cdot \frac{\tau}{\tau + \tau_0} + \left(1 - \frac{\tau}{\tau + \tau_0}\right)\right)} \\ &= \sqrt{\sigma^2 \left(\frac{\sigma_0^2}{\sigma_0^2 + \sigma^2} + 1\right)} \\ &= \sqrt{1 + ICC} \cdot \sigma \end{aligned}$$

□

**Corollary 7.1.1.** *Under the assumption that  $ICC \rightarrow 1$ , the marginal distribution of the change in biomarker measurement,  $d = y - y_0$ , given a dataset of double-baseline measurements,  $\mathbf{d}_b = \{d_{b1}, d_{b2}, \dots, d_{bN_b}\}$  where  $d_{bj} = y_{bj2} - y_{bj1}$ , is a Student-t distribution:*

$$p(d|\mathbf{d}_b, M_0) = \text{St}\left(\sqrt{d^2/\bar{d}_b^2}, N_b\right)$$

where  $\bar{d}_b^2 = \frac{1}{N_b} \sum_j d_{bj}^2$

*Proof.* Again to make notation simpler we use the precision of the measurement system  $\tau = \frac{1}{\sigma^2}$  such that according to equation 9 the distribution of repeat baseline difference is given by

$$p(d_{bj}|\tau) = \mathcal{N}\left(0, \sqrt{\frac{2}{\tau}}\right)$$

when  $ICC = 1$ . To determine the posterior probability of  $\tau$  we use Bayes' theorem such that

$$\begin{aligned} p(\tau|\mathbf{d}_b) &\propto p(\tau)p(\mathbf{d}_b|\tau) \\ &= p(\tau) \prod_{j=1}^{N_b} p(d_{bj}|\tau) \end{aligned}$$

Using a non-informative prior  $p(\tau) \propto \tau^{-1}$  we obtain:

$$p(\tau|\mathbf{d}_b) \propto \tau^{N_b/2-1} \exp\left\{-\frac{\tau}{2} \sum_{j=1}^{N_b} d_{bj}^2\right\}$$

Marginalizing over  $\tau$  thus provides the distribution of the change in measurement after treatment conditioned on the repeatability data:

$$\begin{aligned} p(d|\mathbf{d}_b) &= \int_0^\infty p(d|\tau)p(\tau|\mathbf{d}_b)d\tau \\ &\propto \int_0^\infty \tau^{1/2} \exp\left\{-\frac{\tau}{2}d^2\right\} \tau^{N_b/2-1} \exp\left\{-\frac{\tau}{2}\sum_{j=1}^{N_b} d_{bj}^2\right\} d\tau \\ &\propto \int_0^\infty \tau^{(N_b-1)/2} \exp\left\{-\frac{\tau}{2}\left(d^2 + \sum_{j=1}^{N_b} d_{bj}^2\right)\right\} d\tau \end{aligned}$$

Using the result

$$\int_0^\infty \tau^A e^{-B\tau} d\tau = \frac{\Gamma(A+1)}{B^{A+1}}$$

where the necessary conditions  $A > -1$  and  $\text{Re}(B) > 0$  are guaranteed by the data, we arrive at

$$\begin{aligned} p(d|\mathbf{d}_b) &\propto \left(d^2 + \sum_{j=1}^{N_b} d_{bj}^2\right)^{-\frac{N_b+1}{2}} \\ &= \left(d^2 + N_b \overline{d_b^2}\right)^{-\frac{N_b+1}{2}} \\ &\propto \left(\frac{d^2/\overline{d_b^2}}{N_b} + 1\right)^{-\frac{N_b+1}{2}} \end{aligned}$$

where

$$\overline{d_b^2} = \frac{1}{N_b} \sum_{i=1}^{N_b} d_{bj}^2$$

We notice from its functional form that this is a Student t distribution

$$\text{St}(t; \nu) = \frac{\Gamma\left(\frac{\nu+1}{2}\right)}{\sqrt{\nu\pi}\Gamma\left(\frac{\nu}{2}\right)} \left(\frac{t^2}{\nu} + 1\right)^{-\frac{\nu+1}{2}}$$

with  $t^2 = d^2/\overline{d_b^2}$  and  $\nu = N_b$ . □

**Theorem 7.2.** *The natural logarithm of the Bayes factor for a measured post-treatment change  $d_y = y_1 - y_0$ , in the case of normally distributed variables with **known** model  $M_1$  parameters  $\mu_\Delta$ ,  $\sigma_\Delta$ , and  $\sigma$  is*

$$\ln(BF_{10}) = \frac{1}{2} \left( \ln(1-\eta) - (1-\eta) \left( \frac{d_y - \mu_\Delta}{\sqrt{2}\sigma} \right)^2 + \left( \frac{d_y}{\sqrt{2}\sigma} \right)^2 \right)$$

where

$$\eta = \frac{\sigma_\Delta^2}{\sigma_\Delta^2 + 2\sigma^2}$$

*Proof.* We use the approach of Savage and Dickey Wagenmakers et al. [2010]. Firstly, we make the substitutions  $\tau = \frac{1}{\sigma^2}$  and  $\tau_\Delta = \frac{1}{\sigma_\Delta^2}$ . Next we note that model  $M_0$  is a special case of  $M_1$  where  $d_x = x_1 - x_0 = 0$ , such that

$$\begin{aligned} BF_{10} &= \frac{p(d_y|M_1)}{p(d_y|d_x=0, M_1)} \\ &= \frac{\int p(d_y|\tau, \mu_\Delta, \tau_\Delta, M_1)p(\tau, \mu_\Delta, \tau_\Delta|M_1)d\tau d\mu_\Delta d\tau_\Delta}{\int p(d_y|d_x=0, \tau, \mu_\Delta, \tau_\Delta, M_1)p(\tau, \mu_\Delta, \tau_\Delta|M_1)d\tau d\mu_\Delta d\tau_\Delta} \end{aligned}$$

However, if we can assume that parameters  $\tau$ ,  $\mu_\Delta$ , and  $\tau_\Delta$  are known, then we can instead write

$$BF_{10} = \frac{p(d_y|\tau, \mu_\Delta, \tau_\Delta, M_1)}{p(d_y|d_x = 0, \tau, \mu_\Delta, \tau_\Delta, M_1)}$$

which by Bayes' theorem becomes

$$\begin{aligned} BF_{10} &= \frac{p(d_x = 0|\mu_\Delta, \tau_\Delta, M_1)p(d_y|\tau, \mu_\Delta, \tau_\Delta, M_1)}{p(d_x = 0|d_y, \tau, \mu_\Delta, \tau_\Delta, M_1)p(d_y|\tau, \mu_\Delta, \tau_\Delta, M_1)} \\ &= \frac{p(d_x = 0|\mu_\Delta, \tau_\Delta, M_1)}{p(d_x = 0|d_y, \tau, \mu_\Delta, \tau_\Delta, M_1)} \end{aligned} \quad (10)$$

Under the assumption that variables are real and normally distributed we have that  $p(d_x|\mu_\Delta, \tau_\Delta, M_1) = \mathcal{N}(\mu_\Delta, 1/\sqrt{\tau_\Delta})$  and so to find the numerator of equation 10 we write

$$p(d_x = 0|\mu_\Delta, \tau_\Delta, M_1) = \sqrt{\frac{\tau_\Delta}{2\pi}} \exp\left\{-\frac{1}{2}\tau_\Delta\mu_\Delta^2\right\}$$

Next we identify

$$p(d_x|d_y, \tau, \mu_\Delta, \tau_\Delta, M_1) \propto p(d_y|d_x, \tau, M_1)p(d_x|\mu_\Delta, \tau_\Delta, M_1)$$

Using the result  $p(d_y|d_x, \tau, M_1) = \mathcal{N}(d_x, \sqrt{2/\tau})$  we obtain

$$\begin{aligned} &p(d_x|d_y, \tau, \mu_\Delta, \tau_\Delta, M_1) \\ &\propto \exp\left\{-\frac{\tau}{4}(d_y - d_x)^2\right\} \exp\left\{-\frac{\tau_\Delta}{2}(d_x - \mu_\Delta)^2\right\} \\ &\propto \exp\left\{-\frac{1}{4}(\tau + 2\tau_\Delta)d_x^2 + \frac{1}{2}(\tau d_y + 2\tau_\Delta\mu_\Delta)d_x\right\} \\ &\propto \exp\left\{-\frac{1}{4}(\tau + 2\tau_\Delta)\left(d_x - \frac{\tau d_y + 2\tau_\Delta\mu_\Delta}{\tau + 2\tau_\Delta}\right)^2\right\} \end{aligned}$$

which we recognise as another normal distribution:

$$p(d_x|d_y, \tau, \mu_\Delta, \tau_\Delta, M_1) = \mathcal{N}\left(\frac{\tau d_y + 2\tau_\Delta\mu_\Delta}{\tau + 2\tau_\Delta}, \sqrt{\frac{2}{\tau + 2\tau_\Delta}}\right)$$

such that

$$\begin{aligned} &p(d_x = 0|d_y, \tau, \mu_\Delta, \tau_\Delta, M_1) = \\ &\sqrt{\frac{\tau + 2\tau_\Delta}{4\pi}} \exp\left\{-\frac{1}{4}\frac{(\tau d_y + 2\tau_\Delta\mu_\Delta)^2}{\tau + 2\tau_\Delta}\right\} \end{aligned}$$

Finally the Bayes Factor is derived as

$$\begin{aligned} BF_{10} &= \frac{p(d_x = 0|\mu_\Delta, \tau_\Delta, M_1)}{p(d_x = 0|d_y, \tau, \mu_\Delta, \tau_\Delta, M_1)} \\ &= \sqrt{\frac{2\tau_\Delta}{\tau + 2\tau_\Delta}} \exp\left\{\frac{1}{4}\left(\frac{(\tau d_y + 2\tau_\Delta\mu_\Delta)^2}{\tau + 2\tau_\Delta} - 2\tau_\Delta\mu_\Delta^2\right)\right\} \\ &= \sqrt{\frac{2\tau_\Delta}{\tau + 2\tau_\Delta}} \exp\left\{\frac{1}{4}\frac{\tau^2 d_y^2 + 4\tau d_y \tau_\Delta \mu_\Delta - 2\tau \tau_\Delta \mu_\Delta^2}{\tau + 2\tau_\Delta}\right\} \\ &= \sqrt{\frac{2\tau_\Delta}{\tau + 2\tau_\Delta}} \exp\left\{-\frac{\tau}{4}\frac{2\tau_\Delta}{\tau + 2\tau_\Delta}(d_y - \mu_\Delta)^2\right\} \exp\left\{\frac{1}{4}\tau d_y^2\right\} \end{aligned}$$

Replacing precision terms with their respective error terms we have

$$BF_{10} = \sqrt{1 - \eta} \exp\left\{-\frac{1}{2}(1 - \eta)\left(\frac{d_y - \mu_\Delta}{\sqrt{2\sigma}}\right)^2\right\} \exp\left\{\frac{1}{2}\left(\frac{d_y}{\sqrt{2\sigma}}\right)^2\right\}$$

where

$$\eta = \frac{\sigma_{\Delta}^2}{\sigma_{\Delta}^2 + 2\sigma^2}$$

which in log form becomes

$$\ln(BF_{10}) = \frac{1}{2} \left( \ln(1 - \eta) - (1 - \eta) \left( \frac{d_y - \mu_{\Delta}}{\sqrt{2}\sigma} \right)^2 + \left( \frac{d_y}{\sqrt{2}\sigma} \right)^2 \right)$$

□

**Corollary 7.2.1.** *The expected values of equation 7 under the assumption of models  $M_0$  or  $M_1$  are*

$$\begin{aligned} \mathbb{E}_{d_y|M_0} \{\ln(BF_{10})\} &= \frac{1}{2} (\ln(1 - \eta) + \eta - (1 - \eta)\xi^2) \\ \mathbb{E}_{d_y|M_1} \{\ln(BF_{10})\} &= \frac{1}{2} \left( \ln(1 - \eta) + \frac{\eta}{1 - \eta} + \xi^2 \right) \end{aligned}$$

where  $\xi = |\mu_{\Delta}|/\sqrt{2}\sigma$ .

*Proof.* If we then investigate the expectation of this value over some distribution of  $d_y$ :

$$\begin{aligned} &\mathbb{E} \{\ln(BF_{10})\} \\ &= \frac{1}{2} \left( \ln(1 - \eta) - \frac{1 - \eta}{2\sigma^2} \mathbb{E} \{(d_y - \mu_{\Delta})^2\} + \frac{1}{2\sigma^2} \mathbb{E} \{d_y^2\} \right) \\ &= \frac{1}{2} \left( \ln(1 - \eta) + \frac{\eta}{2\sigma^2} \mathbb{E} \{d_y^2\} + \frac{1 - \eta}{2\sigma^2} \mu_{\Delta} (2\mathbb{E}\{d_y\} - \mu_{\Delta}) \right) \end{aligned}$$

Considering that

$$\begin{aligned} p(d_y|\sigma, \mu_{\Delta}, \sigma_{\Delta}, M_0) &= \mathcal{N}(0, \sqrt{2}\sigma) \\ \Rightarrow \mathbb{E}_{d_y|M_0}(d_y) &= 0 \quad \text{and} \quad \mathbb{E}_{d_y|M_0}(d_y^2) = 2\sigma^2 \end{aligned}$$

and

$$\begin{aligned} p(d_y|\sigma, \mu_{\Delta}, \sigma_{\Delta}, M_1) &= \mathcal{N}\left(\mu_{\Delta}, \sqrt{2\sigma^2 + \sigma_{\Delta}^2}\right) \\ \Rightarrow \mathbb{E}_{d_y|M_1}(d_y) &= \mu_{\Delta} \quad \text{and} \quad \mathbb{E}_{d_y|M_1}(d_y^2) = \mu_{\Delta}^2 + 2\sigma^2 + \sigma_{\Delta}^2 \end{aligned}$$

we have that

$$\begin{aligned} \mathbb{E}_{d_y|M_0} \{\ln(BF_{10})\} &= \frac{1}{2} (\ln(1 - \eta) + \eta - (1 - \eta)\xi^2) \\ \mathbb{E}_{d_y|M_1} \{\ln(BF_{10})\} &= \frac{1}{2} \left( \ln(1 - \eta) + \frac{\eta}{1 - \eta} + \xi^2 \right) \end{aligned}$$

□

## 7.2 Sensitivity Analysis Results for Study 2

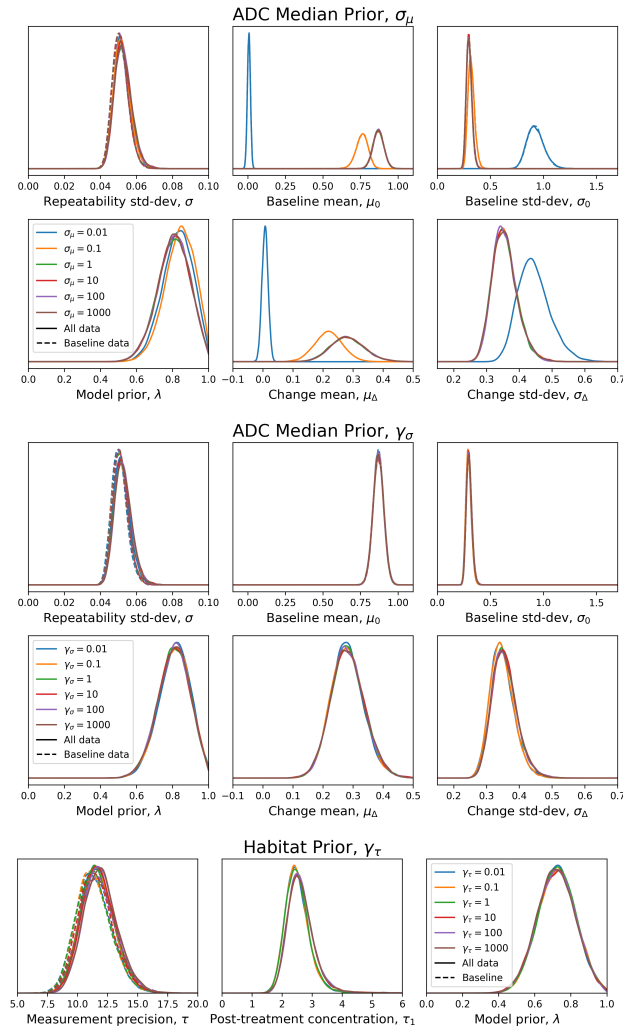


Figure 12: Prior sensitivity analysis for Study 2. The only prior parameter that had significant impact on posterior distributions were low values of  $\sigma_\mu$ , which represents the width of the zero-mean normal prior for  $\mu_0$  and  $\mu_\Delta$  in ADC median biomarkers. For ADC median biomarkers, other than  $\lambda$ , all values have units  $\times 10^{-3} \text{ mm}^2/\text{s}$ .

### 7.3 Median ADC Stan Code

Below we present the Stan code that was used for inference of the model for median ADC estimates (real values).

```

data {
  int <lower=1> Nb;           // Number of repeat baseline data
  int <lower=1> Np;           // Number of post-treatment data
  vector[Nb] yb1;           // Baseline measurement 1
  vector[Nb] yb2;           // Baseline measurement 2
  vector[Np] yp1;           // Post-treatment measurement 1
  vector[Np] yp2;           // Post-treatment measurement 2
  real <lower=0> sd_prior;   // Prior width for std-devs (gamma)
  real <lower=0> mu_prior;   // Prior width for means
}

transformed data {
  vector[Nb] db = yb2 - yb1;
  vector[Nb] mb = (yb1 + yb2) / 2;
  vector[Np] dp = yp2 - yp1;
}

parameters {
  real <lower=0> sdr;         // Measurement error
  real <lower=0> sd0;         // Std-dev of baseline
  real <lower=0> sdd;         // Std-dev of differences
  real mu0;                  // Population baseline value
  real mud;                  // Population mean difference
  real <lower=0, upper=1> lambda; // Mixing proportion
}

model {
  // Priors
  sdr ~ cauchy(0, sd_prior);
  sd0 ~ cauchy(0, sd_prior);
  sdd ~ cauchy(0, sd_prior);
  mu0 ~ normal(0, mu_prior);
  mud ~ normal(0, mu_prior);
  lambda ~ uniform(0, 1);

  // repeat baseline likelihood
  db ~ normal(0, sqrt(2) * sdr);
  mb ~ normal(mu0, sqrt(square(sd0) + square(sdr)/2));

  // post-treatment likelihood
  vector[Np] lp0;
  vector[Np] lp1;
  for (n in 1:Np) {
    lp0[n] = loglm(lambda) +
      normal_lpdf(dp[n] | 0, sqrt(2) * sdr);
    lp1[n] = log(lambda) +
      normal_lpdf(dp[n] | mud,
        sqrt(square(sdd) + square(sdr) * 2));
  }
  target += sum(log_sum_exp(lp0, lp1));
}

generated quantities {
  vector[Np] z;             // Model label samples
  for (n in 1:Np){
    real lp0 = loglm(lambda) +
      normal_lpdf(dp[n] | 0, sqrt(2) * sdr);
    real lp1 = log(lambda) +
      normal_lpdf(dp[n] | mud,
        sqrt(square(sdd) + square(sdr) * 2));
    z[n] = categorical_rng([exp(lp0 - log_sum_exp(lp0, lp1)),
      exp(lp1 - log_sum_exp(lp0, lp1))]');
  }
}

```

## 7.4 Dirichlet-Multinomial Stan Code

Below we present the Stan code that was used for inference of the model for habitat estimates (Dirichlet-Multinomial variates).

```

functions {
  vector dir_mult(array[,] int y, vector mu, real prec) {
    int N = dims(y)[1];
    int K = dims(y)[2];
    vector[N] y_sum = to_vector(rep_array(0, N));
    vector[N] p_sum = to_vector(rep_array(0, N));
    for (k in 1:K) {
      vector[N] y_col = to_vector(y[:, k]);
      y_sum += y_col;
      p_sum += lgamma(y_col + mu[k] * prec);
    }
    return lgamma(prec) -
      lgamma(y_sum + prec) +
      p_sum - sum(lgamma(mu * prec));
  }

  real dir_mult_lpmf(array[,] int y, vector mu, real prec) {
    return sum(dir_mult(y, mu, prec));
  }
}

data {
  int <lower=2> K;           // Number of components
  int <lower=1> Nb;         // Number of repeat baseline data
  int <lower=1> Np;         // Number of post-treatment data
  simplex[K] mu0;         // Known mean pre-treatment value
  array[Nb, K] int <lower=0> yb; // Repeat baseline measurements
  array[Np, K] int <lower=0> yp; // Study measurements
  real <lower=0> prec_prior; // Prior width for precision (gamma)
}

parameters {
  real<lower=0> prec;       // Precision of the measurement
  real<lower=0> conc;       // Concentration of the changes
  simplex[K] mu1;         // Population average of changes
  real<lower=0, upper=1> lambda; // Mixing proportion
}

model {
  // Priors
  prec ~ cauchy(0, prec_prior);
  conc ~ cauchy(0, prec_prior);
  lambda ~ uniform(0, 1);
  mu1 ~ dirichlet(rep_vector(1, K));

  // Repeat Baseline Likelihood
  yb ~ dirichlet_multinomial(mu0, prec);

  // Post-treatment Likelihood
  vector[Np] lp0;
  vector[Np] lp1;
  for (n in 1:Np) {
    lp0[n] = log1m(lambda) + dir_mult_lpmf(yp[n] | mu0 * prec);
    lp1[n] = log(lambda) + dir_mult_lpmf(yp[n] | mu1 * conc);
  }
  target += sum(log_sum_exp(lp0, lp1));
}

generated quantities {
  vector[Np] z;           // Model label samples
  for (n in 1:Np) {
    real lp0 = log1m(lambda) + dir_mult_lpmf(yp[n] | mu0 * prec);
    real lp1 = log(lambda) + dir_mult_lpmf(yp[n] | mu1 * conc);
    z[n] = categorical_rng([exp(lp0 - log_sum_exp(lp0, lp1)),
                          exp(lp1 - log_sum_exp(lp0, lp1))]');
  }
}

```